

# 1 Feasibility of robust estimates of ozone production rates 2 using a synergy of satellite observations, ground-based 3 remote sensing, and models

4  
5 Amir H. Souri<sup>1,2\*</sup>, Gonzalo González Abad<sup>3</sup>, Glenn M. Wolfe<sup>1</sup>, Tijl Verhoelst<sup>4</sup>, Corinne Vigouroux<sup>4</sup>,  
6 Gaia Pinardi<sup>4</sup>, Steven Compernelle<sup>4</sup>, Bavo Langerock<sup>4</sup>, Bryan N. Duncan<sup>1</sup>, Matthew S. Johnson<sup>5</sup>

7  
8 <sup>1</sup>Atmospheric Chemistry and Dynamics Laboratory, NASA Goddard Space Flight Center, Greenbelt, MD,  
9 USA

10 <sup>2</sup>GESTAR II, Morgan State University, Baltimore, MD, USA

11 <sup>3</sup>Atomic and Molecular Physics (AMP) Division, Center for Astrophysics | Harvard & Smithsonian,  
12 Cambridge, MA, USA

13 <sup>4</sup>Royal Belgian Institute for Space Aeronomy (BIRA-IASB), Ringlaan 3, 1180 Uccle, Belgium

14 <sup>5</sup>Earth Science Division, NASA Ames Research Center, Moffett Field, CA, USA

15 \* Corresponding author: [a.souri@nasa.gov](mailto:a.souri@nasa.gov)

## 16 17 **Abstract.**

18 Ozone pollution is secondarily produced through a complex, non-linear chemical process. Our  
19 understanding of the spatiotemporal variations in photochemically produced ozone (i.e., PO<sub>3</sub>) is limited to  
20 sparse aircraft campaigns and chemical transport models, which often carry significant biases. Hence, we  
21 present a novel satellite-derived PO<sub>3</sub> product informed by bias-corrected TROPOMI HCHO, NO<sub>2</sub>, surface  
22 albedo data, and various models. These data are integrated into a parameterization that relies on HCHO,  
23 NO<sub>2</sub>, HCHO/NO<sub>2</sub>, jNO<sub>2</sub>, and jO<sup>1</sup>D. Despite its simplicity, it can reproduce ~90% of the variance in  
24 observationally constrained PO<sub>3</sub> with minimal biases in moderately to highly polluted regions. We map PO<sub>3</sub>  
25 across various regions in July 2019 at a 0.1°×0.1° spatial resolution, revealing accelerated values (>8  
26 ppbv/hr) in numerous cities throughout Asia and the Middle East, resulting from the elevated ozone  
27 precursors and enhanced photochemistry. In Europe and the United States, such high levels are only  
28 detected over Benelux, Los Angeles, and New York City. PO<sub>3</sub> maxima are seen in various seasons, attributed  
29 to changes in photolysis rates, non-linear ozone chemistry, and fluctuations in HCHO and NO<sub>2</sub>. Satellite  
30 errors result in moderate errors (10-20%) of PO<sub>3</sub> estimates over cities on a monthly average, while these  
31 errors exceed 50% in clean areas and under low light conditions. Using the current algorithm, we have  
32 demonstrated that satellite data can provide valuable information for robust PO<sub>3</sub> estimation. This capability  
33 expands future research through the application of data to address significant scientific questions about the  
34 locally-produced PO<sub>3</sub> hotspots, seasonality, and long-term trends.

## 35 **1. Introduction**

36 Tropospheric ozone (O<sub>3</sub>) is a secondary pollutant formed through complex photochemical reactions  
37 involving various precursors, including nitrogen oxides (NO<sub>x</sub> = NO + NO<sub>2</sub>), volatile organic compounds

38 (VOCs), aerosols, and halogens (Kleinman et al., 2002, Simpson et al., 2015; Li et al., 2019). Ozone not  
39 only poses significant risks to human health (Fleming et al., 2018) and agricultural productivity (Mills et  
40 al., 2018) but also influences the radiation budget, thereby affecting the climate (Gaudel et al., 2018). To  
41 mitigate the problem of elevated locally-produced ozone, it is crucial to understand the spatiotemporal  
42 variability in ozone production rates ( $PO_3$ ), defined as the number of ozone molecules generated through  
43 secondary chemical pathways in the atmosphere. Comprehensive studies of ozone chemistry, informed by  
44 observations, are typically confined to observationally-rich air quality campaigns (e.g., Cazorla et al., 2012;  
45 Ren et al., 2013; Mazzuca et al.; 2016; Souri et al., 2020a; Schroeder et al., 2020; Brune et al., 2022; Wolfe  
46 et al., 2022; Souri et al., 2023), which are sparse in time and space.

47 Significant advancements have been achieved in using various measurable ozone indicators to  
48 simplify the non-linear relationship between  $PO_3$  and  $NO_x$  and VOCs into linear forms (Sillman and He,  
49 2002). These forms include  $NO_x$ -sensitive (where  $PO_3$  is sensitive to  $NO_x$ ), VOC-sensitive (where  $PO_3$  is  
50 sensitive to VOCs), and the transitional regimes (where  $PO_3$  is sensitive to both  $NO_x$  and VOCs). Among  
51 the numerous proposed indicators, the ratio of formaldehyde (HCHO) to nitrogen dioxide ( $NO_2$ ) (known as  
52 FNR) has gained popularity (Tonnesen and Dennis, 2000a,b), despite its less effective performance  
53 compared to the  $H_2O_2/HNO_3$  ratio in fully explaining the  $HO_x$ - $RO_x$  cycle (Sillman and He, 2002; Souri et  
54 al., 2023). The preference for FNR stems from the fact that both quantities can be informed by UV-Vis  
55 radiance data, such as those provided by the Ozone Monitoring Instrument (OMI) and the TROPospheric  
56 Monitoring Instrument (TROPOMI) (Martin et al., 2005; Duncan et al., 2010; Choi et al., 2012; Choi and  
57 Souri, 2015a, b; Jin and Holloway, 2015; Jin et al., 2017; Schroeder et al., 2017; Souri et al., 2017; Jeon et  
58 al., 2018; Tao et al., 2022). Several limitations associated with the application of satellite-based FNR have  
59 been identified such as i) the inherent limitation of understanding the radical termination in the  $RO_x$ - $HO_x$   
60 cycle (Souri et al., 2020a; Souri et al., 2023), ii) the challenges associated with converting the column  
61 vertical density to the near-surface concentrations (Jin et al., 2017; Schroeder et al., 2017; Souri et al.,  
62 2023), iii) spatial representativity associated with large satellite pixels (Souri et al., 2020a, 2023; Johnson  
63 et al., 2023), and iv) the retrieval errors (Souri et al., 2023; Johnson et al., 2023). Souri et al. (2023)  
64 concluded that the retrieval errors make up the largest portion of total errors associated with FNR. These  
65 errors are becoming smaller with better sensor designs, retrieval algorithms, and calibration over time.

66 While the characterization of ozone regimes offers valuable insights for regulators to prioritize  
67 effective emission control strategies, it does not provide information about the magnitude of  $PO_3$  or the  
68 absolute quantities of  $PO_3$  derivatives relative to its precursors. Consequently, chemical transport models  
69 under various emission scenarios are typically employed (e.g., Pan et al., 2019). These models allow for  
70 the execution of process-based scenarios to elucidate the response of  $PO_3$  to different emissions and can  
71 simulate four-dimensional  $PO_3$  data. However, the results of these simulations are based on various  
72 assumptions and inputs, which carry significant uncertainties. Therefore, it is essential to optimize some of  
73 the models' prognostic inputs using observations through inverse modeling/data assimilation. The primary  
74 advantage of inverse modeling/data assimilation using satellite observations is its ability to account for  
75 satellite errors and eliminate the influence of the a priori profile, thereby carrying only radiance information  
76 into the emission estimation. Numerous studies have utilized satellite observations to constrain  $NO_x$  and  
77 VOC emissions for various applications (e.g., Stavrakou et al., 2016; Souri et al., 2016; Miyazaki et al.,  
78 2017; Souri et al., 2017; Souri et al., 2020b; Souri et al., 2021; Choi et al., 2022; DiMaria et al., 2023).  
79 Souri et al. (2020b) made an early attempt to simultaneously optimize both  $NO_x$  and VOC emissions over  
80 East Asia for a more accurate representation of  $PO_3$ . Their joint-inversion was able to account for the  
81 intertwined relationship between HCHO- $NO_x$  and  $NO_2$ -VOC. However, the execution of chemical transport  
82 models optimized by multiple satellite observations remains prohibitively expensive, particularly for high-  
83 resolution domains demanded by regulatory agencies.

84 Data-driven methods for estimating  $PO_3$  can become as a more cost-effective alternative to physics-  
85 based methods. While using constrained chemical transport models provides a relatively robust framework  
86 grounded in some explicit governing equations, they require extensive computation resources and expertise.

87 Conversely, data-driven algorithms make use of large datasets to identify patterns and make predictions  
88 with much reduced computational expenses. However, it is important to recognize that data-driven  
89 algorithms lack the ability to provide solid physical interpretability and generalizability. Despite this  
90 fundamental limitation, they are sensible tools for applications where rapid analysis over a wide spatial  
91 coverage is prioritized. Data-driven parameterizations for several components of atmospheric chemistry  
92 such as OH (Anderson et al., 2022) and dry deposition (Silva et al., 2019) have been crafted for this reason.  
93 However, to our best knowledge, Chatfield et al. (2010) and Souri et al. (2023) are the only studies that  
94 attempted to empirically parameterize PO<sub>3</sub> using the information of HCHO and NO<sub>2</sub> mixing ratios.

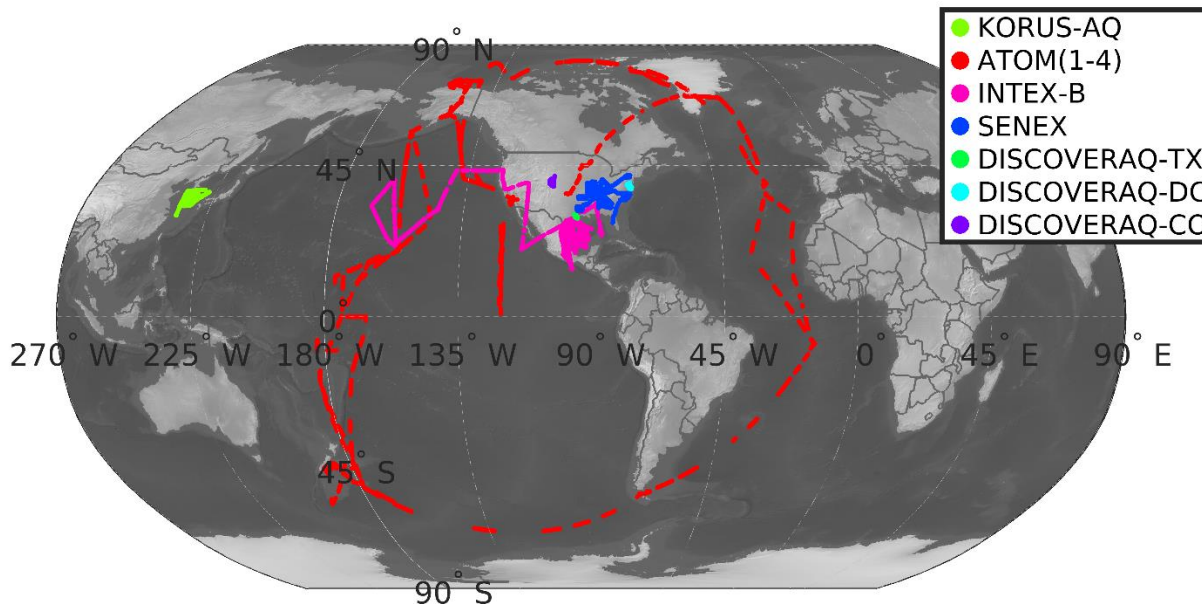
95 Inspired by those works, we developed a novel product using TROPOMI observations in  
96 conjunction with **ground-based remote sensing** and atmospheric models to **estimate** PO<sub>3</sub> and associated  
97 errors within the planetary boundary layer (PBL) across the globe. This enabled us to map PO<sub>3</sub> across  
98 various regions at fine scales (i.e., 0.1°×0.1°) for the first time.

## 99 **2. Data**

### 100 **2.1. Aircraft**

101 To study PO<sub>3</sub>, we use various aircraft observations from several **National Aeronautics and Space**  
102 **Administration** (NASA) and **National Oceanic and Atmospheric Administration** (NOAA) atmospheric  
103 composition campaigns. We have selected three sets of aircraft campaigns for the purpose of PO<sub>3</sub>  
104 estimation, targeting: i) urban/suburban air quality, including Deriving Information on Surface Conditions  
105 from Column and Vertically Resolved Observations Relevant to Air Quality (DISCOVER-AQ) Baltimore-  
106 Washington (2011), DISCOVER-AQ Houston-Texas (2013), DISCOVER-AQ Colorado (2014), and the  
107 Korea United States Air Quality Study (KORUS-AQ) (2016) (Crawford et al., 2021); ii) remote areas  
108 including Atmospheric Tomography Mission (ATOM) (Thompson et al., 2022) and Intercontinental  
109 Chemical Transport Experiment (INTEX) phase B (Singh et al., 2009); iii) a mixture of isoprene-rich  
110 environment and large emitters, including SENEX (Southeast Nexus) (Warneke et al., 2016). Figure 1  
111 shows the location of these campaigns. Inspired by the study of Miller and Brune (2022), we list their  
112 “when, where, why” characteristics in Table S1.

113 For aircraft campaigns targeting polluted areas, including DISCOVERs, KORUS-AQ, SENEX,  
114 and SEAC4RS, we use 10-sec merged data, whereas, for other measurements taken in relatively remote  
115 areas, such as INTEX-B and ATOMs, we used 30-sec merged data. A more detailed description of the  
116 measurements is provided in Section 3.2. We exclude times with no measurements of NO, NO<sub>2</sub>, or HCHO.  
117 The concentrations of OH and HO<sub>2</sub> were only measured during INTEX-B, ATOMs, and KORUS-AQ.  
118 Likewise, we void any data points lacking either HO<sub>2</sub> or OH measurements. There are frequent gaps in  
119 some measurements, especially for VOCs, because of instrument issues or measurement techniques.  
120 Following Souri et al. (2020a), Miller and Brune (2020), Souri et al. (2023), and Bottorff et al. (2023), we  
121 fill the gaps in measurements using a linear interpolation method with no extrapolation allowed beyond 15  
122 minutes. We drop any remaining gaps from the analysis. To better capture the rapid fluctuation of VOCs,  
123 we pick the PTR-TOF-MS instrument with high temporal resolution over the whole air sampler (WAS)  
124 when both instruments have measured the same quantity. Regarding the INTEX-B campaign, we drop  
125 isoprene observation due to infrequent samples downgrading the performance of our box model.



126  
 127 **Figure 1.** The location of seven different atmospheric composition aircraft campaigns used in this study.

128 **2.2. TROPOMI  $\text{NO}_2$  and HCHO**

129 We use the recently reprocessed daily level-2 (L2) TROPOMI tropospheric  $\text{NO}_2$  and total HCHO  
 130 columns (v2.4) derived from UV-visible radiances onboard the European Space Agency’s (ESA’s) Sentinel-  
 131 5 Precursor (S5P) spacecraft (~328-496 nm) (Veefkind et al., 2012, De Smedt et al. 2021; van Geffen et al.,  
 132 2022). This sensor has been operational since May 2018, providing global coverage of  $\text{NO}_2$  and HCHO at  
 133 ~1:30 local standard time at the Equator. Since  $\text{NO}_2$  and HCHO are optically thin absorbers in the UV-  
 134 Visible, meaning their concentrations do not substantially affect the sensitivity of the radiance to the optical  
 135 thickness of the absorber, the retrieval follows the conventional two-step algorithm involving spectral fitting  
 136 for Slant Column Density (SCD) retrieval and Air Mass Factor (AMF) calculations for SCD to Vertical  
 137 Column Density (VCD) conversion. The product has a spatial resolution of 7.2 km (5.6 km as of August  
 138 2019) by 3.6 km at nadir. To remove unfit measurements, we use the provided quality flag ( $q\_value$ ) and  
 139 choose only those above 0.75 for  $\text{NO}_2$  and 0.5 for HCHO. As the L2 product does not come in a regular  
 140 grid, we use a mass-conserved regridding technique based on barycentric linear interpolation to map out  
 141 the data onto a  $0.1^\circ \times 0.1^\circ$  regular grid.

142 van Geffen et al. (2022) demonstrated that the reprocessed TROPOMI tropospheric  $\text{NO}_2$  columns  
 143 exhibit a good level of correspondence with those obtained from ground-based MAX-DOAS sky  
 144 spectrometers, with a correlation of 0.88 and a median bias of -23%, improving on the older product  
 145 versions which were biased low by about 30% with respect to ground-based measurements at polluted sites  
 146 (Verhoelst et al., 2021). More information about new modifications and their impacts on the retrieval can  
 147 be found in van Geffen et al. (2022).

148 The studies of Vigouroux et al. (2020) and De Smedt et al. (2021) validated the reprocessed  
 149 monthly-mean TROPOMI HCHO columns against FTIR and MAX-DOAS observations and found a good  
 150 correlation above 0.8 with a negative bias of 20-30% for polluted sites. The bias tends to be slightly positive  
 151 or neutral over clean sites.

152 **2.2.1. Error characterization of TROPOMI  $\text{NO}_2$  and HCHO using ground-based retrievals**

153 To propagate TROPOMI retrieval errors to the  $\text{PO}_3$  product and to remove potential biases, we  
 154 assume three origins for errors: i) random errors resulting from instrument noise, ii) a fixed additive

155 component that is magnitude-independent (i.e., a uniform offset persisting over all pixels), and iii)  
 156 unresolved systematic biases that are multiplicative and irreducible by oversampling. The first component  
 157 is derived from the column precision variable provided along with the L2 product. In the spatial domain,  
 158 we interpolate the squares of this error the same of way we map the irregular L2 pixels into the  $0.1^\circ \times 0.1^\circ$   
 159 regular grid. Moreover, we average the random errors over a month to reduce random noise by the squared  
 160 number of pixels available at the same location (Eq. 3). Two other errors are determined by comparing  
 161 FTIR (for HCHO) and MAX-DOAS (for tropospheric  $\text{NO}_2$ ) with TROPOMI data (Section 4.3.3). Detailed  
 162 explanation of how these datasets are paired can be found in Vigouroux et al. (2020) and Verhoelst et al.  
 163 (2021). Both datasets cover the period of 2018-2023.

164 To achieve an optimal linear fit ( $y = ax + b + \varepsilon$ ) between the paired observations, where  $a$  and  $b$   
 165 are slope and offset to be determined, we follow a Monte-Carlo Chi-squares minimization such that  $\chi^2 =$   
 166  $\sum \frac{[y-f(x_i,a,b)]^2}{\sigma_y^2 + a^2 \sigma_x^2}$  is minimized. In this equation,  $\sigma_y^2$  and  $\sigma_x^2$  are the variances of  $y$  (TROPOMI) and  $x$  (the  
 167 benchmark, here FTIR or MAX-DOAS), respectively;  $i$  is the subscript refers to  $i$ -th observation point, and  
 168  $f$  is the proposed linear fit subject to optimization. In terms of TROPOMI  $\text{NO}_2$  and HCHO, the errors are  
 169 populated based on the L2 information. According to Verhoelst et al. (2021), a fixed error of 30% is assumed  
 170 for MAX-DOAS  $\text{NO}_2$  observations whose values are above  $1.4 \times 10^{15} \text{ molec/cm}^2$ . Because of the detection  
 171 limit of MAX-DOAS  $\text{NO}_2$ , we set errors for values below that threshold to  $1.4 \times 10^{15} \text{ molec/cm}^2$ . The FTIR  
 172 retrieval errors described in Vigouroux et al. (2020) were used to populate the errors associated with this  
 173 benchmark. The minimization is performed 10000 times, each with a set of random perturbations of  $x$  and  
 174  $y$  within their respective prescribed errors. This approach allows us to assess the robustness of the estimates  
 175 across the range of errors associated with each data point.

176 The offset (a uniform additive term) and the slope (multiplicative error) drawn from the ground  
 177 validation are used to correct the biases associated with TROPOMI via:

$$VCD_{bias-corrected} = \frac{VCD_{original} - offset}{slope} \quad (1)$$

178 Since there are errors associated with this adjustment resulting from instrument and representation errors,  
 179 we augment errors of the slope and offset to the total error and label them constant errors ( $e_{const}$ ) via:

$$e_{const}^2 = e_{offset}^2 + e_{slope}^2 \times VCD_{bias-corrected}^2 \quad (2)$$

180 where  $e_{offset}^2$  and  $e_{slope}^2$  are squares of errors of offset and slope calculated from the linear regression (Eq.  
 181 1). Ultimately, the sum of all three errors constitutes the total errors given:

$$e^2 = e_{const}^2 + \frac{1}{m^2} \sum_{i=1}^m e_{random,i}^2 \quad (3)$$

182 where  $m$  is the number of samples for a given grid and timeframe and  $e_{random}^2$  is squares of random errors.

### 183 2.3. TROPOMI Surface Albedo

184 To account for the effect of surface albedo on photolysis rates (Section 2.5), we use a newly  
 185 developed algorithm based on the directionally dependent Lambertian-equivalent reflectivity (DLER) UV  
 186 surface albedo climatology made from TROPOMI radiance (Tilstra et al., 2024). This new database  
 187 leverages 60 months of TROPOMI reprocessed radiance and is produced at the grid resolution of  
 188  $0.125^\circ \times 0.125^\circ$ . The product has outperformed traditional LER products such as OMI when both were  
 189 compared to MODIS surface the bidirectional reflectance distribution function (BRDF) results (Tilstra et  
 190 al., 2024).



## 191 2.4. MERRA2-GMI

192 To convert vertical column densities of HCHO and NO<sub>2</sub> from TROPOMI to their volume mixing  
193 ratios in the PBL region, we use the MERRA2-GMI (M2GMI) model ([https://acd-  
194 ext.gsfc.nasa.gov/Projects/GEOSCCM/MERRA2GMI/](https://acd-ext.gsfc.nasa.gov/Projects/GEOSCCM/MERRA2GMI/), last access: 10 Sep 2023). This model is NASA’s  
195 Goddard Earth Observing System (GEOS) Chemistry-Climate Model (CCM) run spanning for the period  
196 of 1980-2019, exploiting MERRA2 (Modern Era Retrospective analysis for Research and Applications) to  
197 constrain meteorological fields (Orbe et al., 2017). The model uses the Global Modeling Initiative (GMI)  
198 chemical mechanism (Duncan et al., 2007; Strahan et al., 2007), which involves over 120 species and 400  
199 reactions. It has a resolution of approximately 0.625° longitude by 0.5° latitude with 72 vertical layers  
200 stretching from the surface up to 0.1 hPa. Additional information about the configuration of this model can  
201 be found in Strode et al. (2019). To carry out the conversion, we apply the following conversion factor ( $\gamma$ )  
202 to the TROPOMI VCDs:

$$\gamma = \frac{\bar{q}_{PBLH}}{\frac{NA}{g \times M_{air}} \sum q dp} \quad (4)$$

203 where  $\bar{q}_{PBLH}$  is the average of the target trace gas mixing ratios in the PBLH,  $g$  is the acceleration  
204 of the gravity (assumed 9.81 m/s<sup>2</sup>),  $NA$  is the Avogadro constant,  $M_{air}$  is the air molecular weight  
205 (assumed 28.96 g/mol),  $q$  is the target trace gas mixing ratio at a given altitude, and  $dp$  is the  
206 thickness of each model vertical grid box in hPa. The denominator in Eq. 4 represents the modeled  
207 VCD. We integrate modeled partial VCDs up to top of the atmosphere for HCHO, and up to the  
208 tropopause pressure layer for NO<sub>2</sub>.

## 209 2.5. TUV NCAR Photolysis Rates Look-up Table

210 To estimate photolysis rates, JNO<sub>2</sub> (NO<sub>2</sub>+hv) and JO<sup>1</sup>D (O<sub>3</sub>+hv), we use a comprehensive look-up  
211 table provided by the F0AM model (Section 3.2) created for clear-sky conditions. This look-up table is  
212 based on the calculation of more than 20,064 solar spectra over a wide range of solar zenith angle (SZA)  
213 (the range [0, 90] in steps of 5°), altitude (the range [0, 15] in steps of 1 km), overhead total ozone column  
214 (the range [100, 600] in steps of 50 DU), and surface UV albedo (the range [0, 1] in steps of 0.2) using  
215 NCAR’s Tropospheric Ultraviolet and Visible radiation model (TUV v5.2) and cross sections and quantum  
216 yields from IUPAC and JPL (Wolfe et al., 2016). The L2 TROPOMI granule information populates SZA,  
217 surface elevation, and surface UV albedo, while overhead total ozone columns are obtained from MERRA2-  
218 GMI (Section 2.4) which is found to agree well with satellite observations (Souri et al., 2024). Any values  
219 between these tables are bilinearly interpolated for a smoother result.

## 220 3. Methods

221 In this section, we begin by discussing a robust regression model specifically developed for  
222 feature selection in the parameterization of PO<sub>3</sub>. We then describe the training dataset created for this  
223 purpose. Following that, we introduce a clustering technique utilized to organize the training data, which  
224 enables us to identify the key drivers of PO<sub>3</sub> variability. Finally, we provide a comprehensive overview of  
225 the PO<sub>3</sub> estimates algorithm by integrating data from the TROPOMI retrievals, ground-based remote  
226 sensing, and various models.

### 227 3.1. LASSO

228 Through the use of multi-linear regression models, it is possible to establish a simple but robust  
229 relationship between multiple variables and a target. However, when dealing with a large number of  
230 variables, there is a chance of introducing overfitting issues. This can lead to predictions that are either  
231 overly optimistic or unrealistic for values outside of the training dataset. To avoid this, it is recommended

232 to simplify the model by removing variables that are loosely connected with the target or highly correlated  
233 with others. This process is known as "model shrinkage" and can narrow down the number of possible  
234 solutions (i.e., variance) at the cost of increasing the biases between the observed target and predictions.  
235 Ideally, we want a model that minimizes the sum of the bias and the variance. To achieve this, we can use  
236 LASSO (least absolute shrinkage and selection operator) (Tibshirani, 1996). They consider a regression,

$$Y = X\beta + \alpha + \varepsilon \quad (5)$$

237 with response  $Y = (y_1, \dots, y_n)^T$ ,  $n \times p$  explanatory variables  $X$ , coefficients  $\beta = (\beta_1, \dots, \beta_p)^T$ , an intercept  $\alpha$ ,  
238 and noise variables  $\varepsilon = (\varepsilon_1, \dots, \varepsilon_n)^T$ .  $n$  is the number of data points, and  $p$  is the number of explanatory  
239 variables. We can label the regression model sparse when many of  $\beta$  values are zero, and we can label it  
240 high dimensional when  $p \gg n$ . LASSO attempts to select variables such that the following cost function is  
241 minimized:

$$(\hat{\alpha}, \hat{\beta}) = \operatorname{argmin} \left\{ \|Y - X\beta - \alpha\|_2 + \lambda \sum_{i=1}^p |\beta_i| \right\} \quad (6)$$

242 where  $\hat{\alpha}$  and  $\hat{\beta}$  are optimized intercept and coefficients,  $\lambda$  is a non-negative regularization factor subject to  
243 tuning,  $i$  is the subscript of the  $i$ -th explanatory variable, and  $\|\cdot\|_2$  is the L2-norm operator. The first term  
244 on the right side of Eq.6 minimizes the squares of the residuals, whereas the second term reduces the sum  
245 of absolute value of coefficients resulting in a simpler model with fewer parameters. Without the second  
246 term, the regression model becomes an ordinary least-squares estimation. The most critical element here is  
247  $\lambda$ . A large  $\lambda$  results in more aggressive regularization leading to more model shrinkage, whereas a small  
248 value preserves a high dimensional model. To optimize this value, we discretize  $\lambda$  in 100 values between  
249  $10^{-4}$  up to  $10^1$ , divide the training dataset into 10 folds (i.e., splitting the dataset into equal size segments),  
250 determine the average of cross-validated error prediction among all folds, and find  $\lambda$  that yields the smallest  
251 error. The final solution ensures a balanced model with respect to model parsimony and bias. All  
252 explanatory variables are standardized during the regularization procedure such that their mean becomes  
253 zero and their standard deviation one.

### 254 3.2. Photochemical box modeling

255 To produce training data sets for LASSO-based  $\text{PO}_3$  estimation, we use the Framework for 0-D  
256 Atmospheric Modeling (F0AM) v4 box model (Wolfe et al., 2016), constrained by a wide range of  
257 observations. These observations ensure that the model achieves a realistic range of values found in the  
258 atmosphere. We follow past setups which apply the Carbon Bond 6 (CB06, r2) chemical mechanism in  
259 F0AM (Souri et al., 2020a; Souri et al., 2023). The model is constrained by aircraft data, including  
260 meteorology, photolysis rates, and trace gas concentrations. The model configuration and observations used  
261 are listed in Table S2.

262 Once the model is initialized and held constant with respect to a wide range of constraining  
263 quantities, it runs at 30 minutes integration time cycling for five days to approach a steady-state  
264 environment. Several key compounds including OH,  $\text{HO}_2$ , HCHO, PAN, NO, and  $\text{NO}_2$  are initialized with  
265 aircraft observations but they are left free to cycle with incoming solar radiation variability. These  
266 compounds play a crucial role in validating the efficacy of model performance as well as the adequacy of  
267 observations used as constraints. In particular, allowing HCHO to vary freely enables us to assess whether  
268 our mechanism for VOC treatment, steady-state, and the number of measured VOCs suffice to reproduce  
269 its concentrations reasonably. Although the individual concentration of  $\text{NO}_2$  and NO are not constrained,  
270 we constrain total  $\text{NO}_x$  ( $\text{NO} + \text{NO}_2$ ). Not all aircraft campaigns measured all photolysis rates included in the  
271 chemical mechanism. We first initialize the photolysis rates included in CB06 using the look-up-tables  
272 described in Section 2.5. If any photolysis reaction rates in CB06 were measured, we replace the initial

273 guess with the observed values. For those reactions with photolysis rates not been measured, we apply a  
274 scaling factor made of the average of the ratio of the observed J-values to the modeled J-values. This  
275 approach is a sensible choice for accounting for large particles such as clouds, as their extinction coefficient  
276 is somewhat non-selective in the UV-Vis range; however, applying a wavelength-independent scaling factor  
277 may introduce some biases for optically complex environments introduced by aerosols.

278 It is essential to acknowledge the inherent limitations of a box model in our research. The model  
279 does not consider the diverse physical loss pathways that trace gases may undergo, including deposition  
280 and transport. As a result, we have simplified the physical loss by employing a first-order dilution rate set  
281 to  $1/86400 \text{ s}^{-1}$ , equivalent to a lifetime of 24 hours. This approach ensures that unconstrained trace gases  
282 that take longer to break down do not accumulate over time. Exact knowledge of dilution factors requires  
283 knowing molecular and turbulent diffusion, entrainment and detrainment, and deposition rates, all of which  
284 are unknown at the micro-scale level of aircraft observations. Nonetheless, studies of Brune et al. (2022)  
285 and Sourì et al. (2023) showed that  $\text{HO}_2$ , OH,  $\text{NO}_x$ , and HCHO are relatively immune to the choice of the  
286 dilution factor, whereas  $\text{RO}_2$  mixing ratios can depart introducing some biases in  $\text{PO}_3$  estimates.

287 We determine simulated  $\text{PO}_3$  by:

$$PO_3 = FO_3 - LO_3 \quad (7)$$

288 where  $\text{LO}_3$  is all possible chemical loss pathways of ozone (negative stoichiometric multiplier matrix) and  
289  $\text{FO}_3$  is all possible chemical pathways producing ozone molecules (positive stoichiometric multiplier  
290 matrix). This calculation is theoretically equivalent to a value obtained from a chemical solver quantifying  
291 the number of ozone molecules produced/lost for each model timestep. The adoption of Eq.7 facilitates the  
292 direct comparison of  $\text{PO}_3$  estimations with those derived from other models, including CTM-based results  
293 (see Figure 10 in Sourì et al., 2021). Furthermore, it allows for a seamless integration of these estimates  
294 into Lagrangian transport models for ozone forecasting purposes.

### 295 3.3. Clustering

296 The aim of using a classifier to group the large quantity and types of aircraft data into similar  
297 features is to allow us to study the primary contributors to  $\text{PO}_3$  under different chemical, solar, and  
298 meteorological conditions. Additionally, this approach will help us understand the range of atmospheric  
299 conditions included in the training dataset. To accomplish this, we employ a widely-used technique known  
300 as  $k$ -means, which has been used in a variety of applications (e.g., Beddows et al., 2009; Sourì et al., 2016b;  
301 Govender and Sivakumar, 2020). In this approach, centroids are distributed randomly throughout a multi-  
302 dimensional dataset, with each centroid representing a distinct class. The algorithm proceeds to assign a  
303 label to each data point by identifying its closest Euclidean distance to the centroids. Following the labeling  
304 of all data points, the algorithm updates the centroids based on the means of the newly-labeled group. This  
305 process continues iteratively until there is minimal change in the location of the centroids. It is worth noting  
306 that  $k$ -means does not guarantee an optimal solution, so we reinitialize the classification 1000 times with a  
307 new set of initial centroids. We select the result with the lowest value for the sum of the Euclidean distance  
308 among data points and centroids to ensure the outcomes are not influenced by random seeding.

309 Redundant features in the input can significantly compromise the effectiveness of the classification,  
310 so we apply principal component analysis (PCA) to the matrix of datasets ( $Z$ ) with  $n$  data points and  $p$   
311 features to reduce the dimension to a PCA-transformed matrix of  $Z$  ( $Z'$ ) with the dimension  $n \times q$ , where  
312  $q < p$ . Despite this reduction in dimension,  $Z'$  preserves a significant variance in  $Z$ , helping us to overcome  
313 the issues of dimensionality or overfitting.

314 We select 11 features simulated by the F0AM model, many of which are set to the observed values,  
315 or their precursors are observationally-constrained. These features are SZA, HCHO/ $\text{NO}_2$ , HCHO $\times\text{NO}_2$ ,  
316 HCHO,  $\text{NO}_2$ , pressure, temperature,  $\text{jNO}_2$ ,  $\text{jO}^1\text{D}$ ,  $\text{H}_2\text{O}$ , and  $\text{NO}_2/\text{NO}_y$  ( $\text{NO}_y = \text{NO} + \text{NO}_2 + \text{PAN} + \text{HNO}_3 + \text{alkyl}$ )

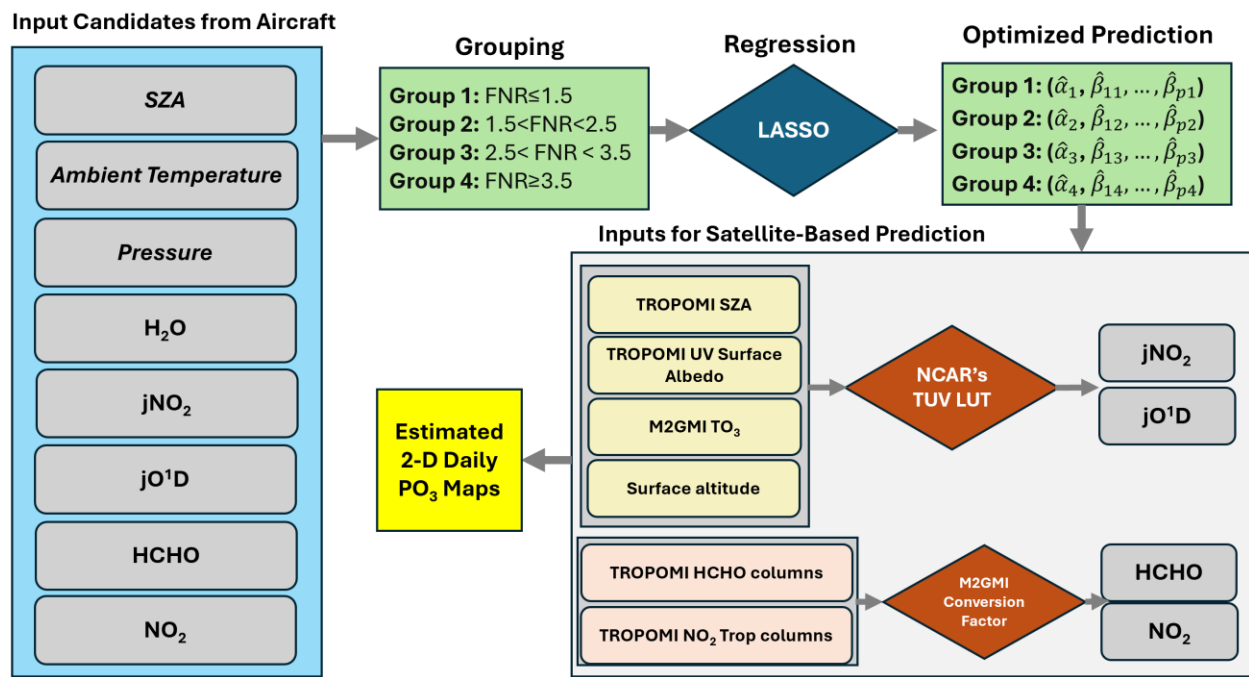


317 nitrate +N<sub>2</sub>O<sub>5</sub>). There are indeed correlations among these features such as SZA and jNO<sub>2</sub>, or HCHO and  
 318 HCHO×NO<sub>2</sub>; nonetheless, we have used PCA to eliminate the possibility of these correlated factors causing  
 319 overfitting issues.

### 320 3.4. The estimation of PO<sub>3</sub>

321 In order to predict PO<sub>3</sub>, we have developed empirical equations using LASSO to link PO<sub>3</sub> with  
 322 various relevant prognostic candidates related to ozone chemistry. A schematic presentation on how this  
 323 estimation can be done to provide daily PO<sub>3</sub> maps at the TROPOMI revisit time across the globe is shown  
 324 in Figure 2. It is important to note that relying solely on linear regressions for a non-linear problem is not a  
 325 viable approach. To address this, we have divided the data points into four distinct groups based on FNR  
 326 values, meaning we divide a non-linear realm into smaller linear segments (i.e., an empirical linearization).  
 327 In a study by Souri et al. (2023), a wide range of aircraft observations and box model results were used to  
 328 determine that FNR~1.7 was a universal threshold for separating NO<sub>x</sub>-sensitive from VOC-sensitive  
 329 regimes. We have found that by breaking down the datapoints into slightly weaker or stronger variations of  
 330 the regimes, we can improve the accuracy of our results. As a result, we have established four distinct  
 331 groups: VOC-sensitive (FNR<1.5), transitions (1.5<FNR<2.5 and 2.5<FNR<3.5), and NO<sub>x</sub>-sensitive  
 332 (FNR>3.5). The coefficients and intercepts based on the LASSO regressions for each group were computed  
 333 separately. From a long list of explanatory parameters, we selected SZA, temperature, pressure, H<sub>2</sub>O, jNO<sub>2</sub>,  
 334 jO<sup>1</sup>D, HCHO, and NO<sub>2</sub> as the most sensible candidates. The reasoning behind this selection will be  
 335 discussed in Section 4.2.

336 Once the LASSO parameters are determined, we apply the linear functions to variables  
 337 modeled/observed in the PBL region. We show that the LASSO method votes for dropping SZA,  
 338 temperature, **water vapor**, and pressure as they do not provide significant information on PO<sub>3</sub> compared to  
 339 the rest. As for jNO<sub>2</sub> and jO<sup>1</sup>D, we use the TUV NCAR’s LUT described in Section 2.5. HCHO and NO<sub>2</sub>  
 340 are **derived by converting** the bias-corrected TROPOMI VCDs into PBL mixing ratios using MERRA2-  
 341 GMI described in Section 2.4. To carry out the conversion, we multiply the satellite VCDs by the ratio of  
 342 averaged modeled mixing ratios of a target gas (i.e., NO<sub>2</sub> or HCHO) in the PBL region divided by modeled  
 343 VCDs (Section 2.4). The PBL field also comes from MERRA2-GMI.



344

345 **Figure 2.** Schematic illustration of daily PO<sub>3</sub> estimation calculated in this study. This process consists of  
346 two major steps: formulating PO<sub>3</sub> as a function of various prognostic inputs derived from the box model  
347 results, and predicting PO<sub>3</sub> based on optimized features/coefficients suggested by LASSO and using  
348 information obtained from TROPOMI, TUV, and M2GMI.

## 349 4. Results and Discussion

### 350 4.1. Box Model Validation

351 In order to assess the accuracy of the assumptions used in the box model's setup, which involves  
352 factors such as chemical mechanism, dilution rate, and photolysis rate correction, we will compare the  
353 simulated values of HCHO, NO<sub>2</sub>, NO, PAN, HO<sub>2</sub>, and OH with their actual measured values. This  
354 comparison will help us determine if our model falls within an acceptable range of errors as seen in other  
355 reputable photochemical box modeling studies. This comparison is represented in Figure 3, which displays  
356 a scatterplot of the data collected from all seven aircraft campaigns. A discussion on each parameter follows:

357 HCHO – The box model is proficient in capturing over 77% of variance in observations with less  
358 than 15% absolute bias. While many box modeling studies prefer to have this compound constrained to  
359 potentially enhance the representation of HO<sub>x</sub>, it comes with the trade-off of hindering us from validating  
360 the number/quality of observed HCHO precursors and/or the VOC treatment. Besides the study of Souri et  
361 al. (2023), Marvin et al. (2017) is one of the few studies that did not constrain this compound to verify the  
362 efficacy of different pathways involved in HCHO formation and loss simulated by various chemical  
363 mechanisms. Marvin et al. (2017) reproduced HCHO formation during the SENEX campaign using the  
364 CB06 mechanism with a R<sup>2</sup>=0.66 and a bias of 32% at 1-min averaged samples. Compared to that study,  
365 we recreate 86% variance in observed HCHO during the same campaign with a bias of 23% (Figure S1) at  
366 10-sec averaged samples. The remaining unresolved variance can be attributed to an incomplete list of VOC  
367 measurements for several campaigns including DISCOVER-AQs and errors of VOCs measurements. It is  
368 unlikely for the chemical mechanism to be reason for this, as Marvin et al. (2017) did not observe substantial  
369 differences in R<sup>2</sup> values among various chemical mechanisms including the near-explicit MCM. A mild  
370 underestimation of HCHO could be likely due to the steady-state assumption, fixed arbitrary dilution factor,  
371 or uncertain isoprene chemistry (Archibald et al., 2000; Wolfe et al., 2016; Marvin et al., 2017).

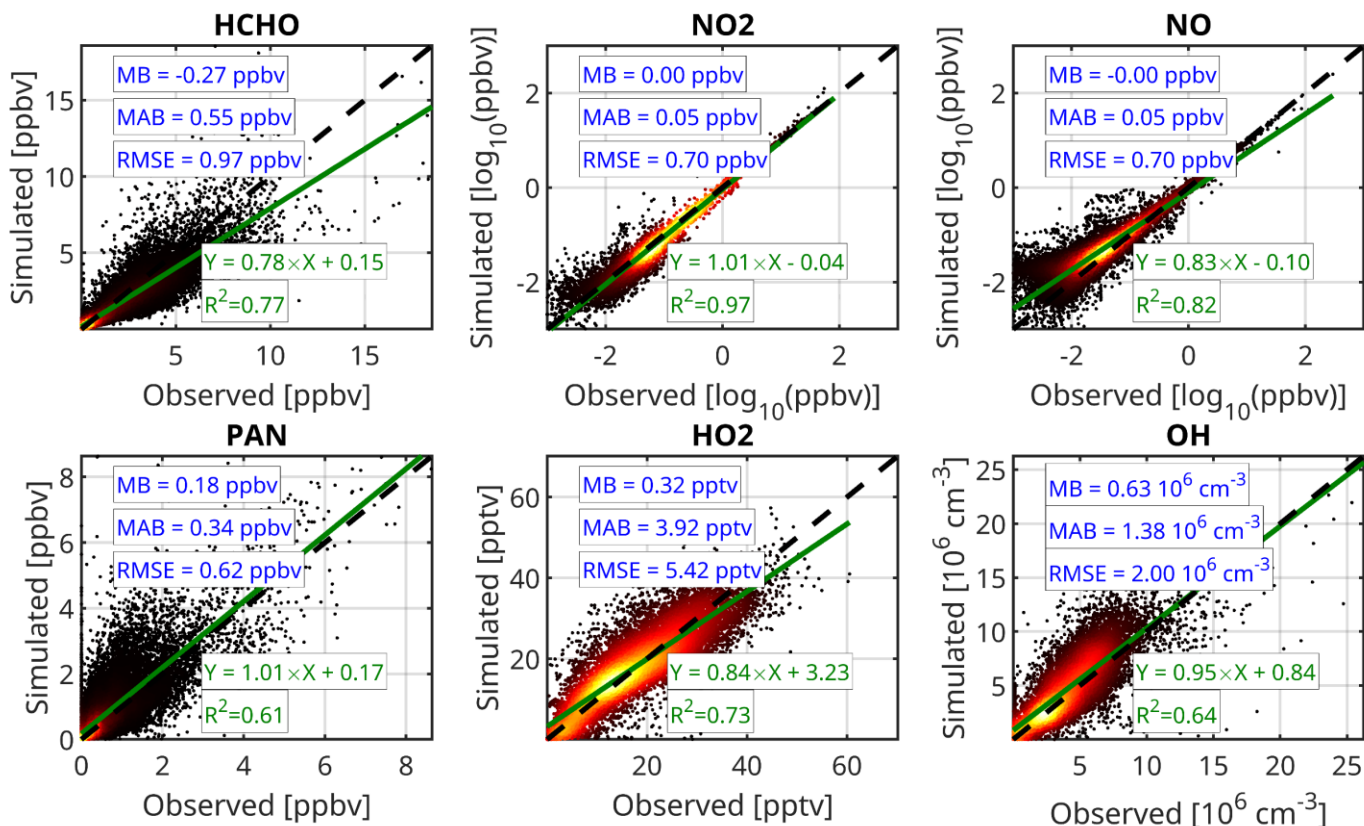
372 NO<sub>2</sub> and NO – Comparisons for both species demonstrate a high degree of correspondence for  
373 values above 0.1 ppbv. Nonetheless, we have noted a substantial amount of fluctuation in the simulations  
374 in clean regions, particularly for NO. While we cannot rule out the possibility of chemical mechanism  
375 uncertainty contributing to this deviation, the reported measurement errors for NO<sub>2</sub> and NO are usually  
376 ±0.05 ppbv and ±0.1 ppbv, respectively. Consequently, it is likely that the measurements error resulted in  
377 more spread in comparison. **In particular, Shah et al. (2023) found that these measurements could be  
378 contaminated by various reactive nitrogen species in remote regions precluding a robust validation of  
379 atmospheric models.**

380 PAN – Our model reproduced 61% of the variance observed in PAN with a marginal absolute bias.  
381 According to Xu et al. (2021), the presence of oxygenated VOCs, particularly acetaldehyde, and the  
382 NO/NO<sub>2</sub> ratio are key factors controlling PAN levels. While we have constrained acetaldehyde, variations  
383 in the NO/NO<sub>2</sub> ratio in heavily polluted regions (where NO<sub>x</sub> levels exceed 1 ppbv) could potentially lead  
384 to biases in PAN simulations. Furthermore, our model's dilution factor has been arbitrarily set, and it is  
385 possible that any bias caused by this factor has been canceled out by other effects, leading to seemingly  
386 bias-free performance. However, Souri et al. (2023) showed that an incorrect dilution factor can  
387 significantly impact PAN performance, causing a sharp decline in R<sup>2</sup> resulting in a value below 30%.  
388 Therefore, the fact that our box model has performed well with respect to PAN could be an indication that  
389 our choice of the dilution factor is **reasonable**.

390 HO<sub>2</sub> and OH – Based on our analysis of HO<sub>2</sub> and OH simulations during KORUS-AQ, INTEX-B,  
391 and ATOMs, we have found a reasonable level of correspondence ( $R^2 > 0.6$ ) with the performance in  
392 previous studies conducted by Sourì et al. (2020), Brune et al. (2022), Miller and Brune (2022), and Sourì  
393 et al. (2023) that focused on some of these campaigns. Although the box model OH simulations reported in  
394 Brune et al. (2019) during ATOMs seemed to be better than ours ( $R^2 \sim 0.8$  vs  $R^2 \sim 0.6$ ), it is important to  
395 consider that their observations were averaged over 1-minute intervals as opposed to our 30-second  
396 intervals. It should also be noted that there can be large errors in ATHOS HO<sub>x</sub> measurements of up to  $\pm 40\%$   
397 (Miller et al., 2022), so recreating the exact variance in the observations should not be the main objective.  
398 Nonetheless, the performance of our simulations in terms of HO<sub>x</sub> compared to observations suggests that  
399 the number of measured compounds and chemical mechanisms used in the model was effective. Our  
400 model's performance with respect to HO<sub>x</sub> is comparable to more sophisticated mechanisms that encompass  
401 a larger number of measured species (Brune et al., 2022; Miller and Brune, 2022).

402 Overall, while there are inevitably some differences between the box model results and  
403 observations, they are consistent with what other studies have found in similar aircraft campaigns. Our  
404 extensive box model results, which consider a variety of meteorological, chemical, and photolysis rates,  
405 demonstrate satisfactory results for unconstrained compounds across a wide range of atmospheric  
406 conditions. This suggests that our training dataset from the box model is a reliable source for understanding  
407 local PO<sub>3</sub>.

408 It is important to note that even if a simulated data point does not match up perfectly with actual  
409 observations, it still plays a role in establishing PO<sub>3</sub> and other explanatory variables. Hypothetically, one  
410 can generate synthetic training data points by running the box model under random numbers for the inputs;  
411 but only a fraction of those can be truly observed in nature. Therefore, a mild outlier in our training dataset  
412 should be viewed as less likely to occur in nature (presuming that these campaigns could represent all  
413 conditions happening in nature), but still a valuable data point drawn from a physical model that can be  
414 used to bridge PO<sub>3</sub> with explanatory variables.



41  
 416 **Figure 3.** The scatterplot comparison of simulations with observed concentrations for six unconstrained  
 417 species. More than ~133,000 observations are used for HCHO, NO<sub>2</sub>, NO, and PAN. HO<sub>x</sub> data points are  
 418 limited to ~55,000 observations. Heat maps show the density of the data. Linear fits are calculated using  
 419 the ordinary least squares method.

420 **4.2. Classification of aircraft data**

421 Following the method described in Section 3.3, we cluster the cloud of aircraft data (~ 133k points)  
 422 into seven distinct classes. We describe them using three categories: pollution level, altitude, and SZA.  
 423 Figure 4 illustrates the violin plot of these classes for various chemical, solar, and meteorological  
 424 conditions. Figure 5 shows their corresponding violin plot of simulated PO<sub>3</sub>. A discussion of each class and  
 425 their relationship to PO<sub>3</sub> follows:

426 C1 (clean, high altitude, high SZA) – Characterized by high altitude flights, cold ambient temperature, and  
 427 negligible water vapor content, this class consists of observations that were typically taken during relatively  
 428 high SZA with a median of 50°. While high altitude observations in clear-sky conditions often should have  
 429 large photolysis rates due to reduced overhead ozone, the relatively high SZA of this class leads to low  
 430 photolysis rates. FNRs tend to be large in this class due to a higher amount of HCHO over NO<sub>2</sub>, and FNP  
 431 (HCHO×NO<sub>2</sub>) and NO<sub>2</sub>/NO<sub>y</sub> ratios are low due to the pristine conditions. The lack of sufficient ozone  
 432 precursors and reduced photochemistry make this class undergo the lowest PO<sub>3</sub> rates with a median of 0.11  
 433 ppbv/hr.

434 C2 (clean, high altitude, low SZA) - This category represents samples collected in low SZA conditions,  
 435 resulting in the highest photolysis rates among all classes. The mass of ozone precursors and the ozone  
 436 sensitivity condition are similar to those in C1. However, C2 PO<sub>3</sub> rates are approximately 60% higher than  
 437 C1 due to increased photochemistry.

438 C3 (moderately clean, medium altitude, high SZA) - This class is characterized by observations collected  
439 in mid-altitudes and high SZA. Airsheds in C3 experienced relatively more polluted air compared to C1  
440 and C2 due to being closer to the surface. Photolysis rates are smaller than C1 possibly because of higher  
441 ozone overhead, although we cannot rule out the varying surface albedo between the classes. Despite the  
442 lower photolysis rates, C3 PO<sub>3</sub> (0.28 ppbv/hr) is larger than that of C2 and C1, indicating that pollution  
443 levels can have a more significant impact than favorable conditions for photochemistry.

444 C4 (moderately clean, medium altitude, low SZA) - This category is distinct from C3 in terms of lower  
445 SZA (resulting in more photochemistry) and a slightly smaller number of ozone precursors. As a result of  
446 the lower ozone precursor concentration, not only is C4 PO<sub>3</sub> (0.19 ppbv/hr) lower than C3, but also is not  
447 different from C2. This again implies that the amount of ozone precursors is more important than the  
448 photochemistry for these conditions.

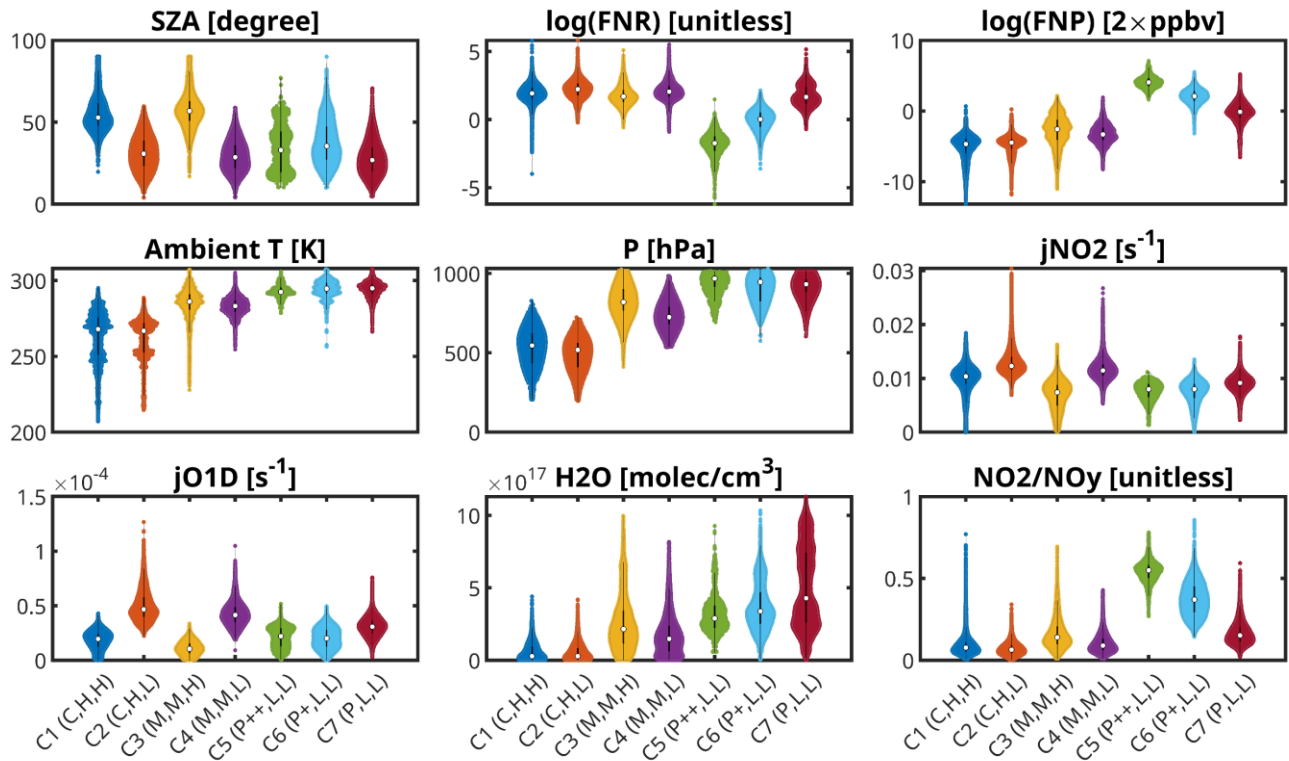
449 C5 (extremely polluted, low altitude, low SZA) - This class features the highest amount of ozone precursors  
450 (median FNP ~ 58 ppbv<sup>2</sup>) among all classes. Furthermore, it is characterized by low photolysis rates due to  
451 its proximity to the surface, and high NO<sub>2</sub>/NO<sub>y</sub> indicative of localized polluted airshed. Unlike the previous  
452 classes, this class has the lowest FNR, indicating that it is mainly located in the VOC-sensitive regime. C5  
453 PO<sub>3</sub> values are much higher than the previous classes, with a value of 3.0 ppbv/hr.

454 C6 (polluted, low altitude, low SZA) - While this class shares similar features with C5 in terms of altitude,  
455 photolysis rates, and meteorology, it experiences a lower FNP (median of 8 ppbv<sup>2</sup>). Despite the lower FNP,  
456 C6 has the highest amount of PO<sub>3</sub> (5.2 ppbv/hr) among all classes. This is a result of reduced non-linearities,  
457 as this class does not often fall into an extreme VOC-sensitive regime (median FNR ~ 1.0) where nitrogen  
458 oxides (NO<sub>x</sub>) can hamper ozone production. This tendency coincides with Souri et al. (2023) which also  
459 found that the highest amount of PO<sub>3</sub>, lied between the transitional regimes, gravitated towards VOC-  
460 sensitive because of abundant ozone precursors and reduced negative chemical feedback of NO<sub>x</sub>.

461 C7 (moderately polluted, low altitude, high SZA) - C7 is characterized by aged air close to the surface with  
462 slightly higher photolysis rates than C5 and C6. C7 PO<sub>3</sub> is 2.5 ppbv/hr, only slightly smaller than C5 despite  
463 much lower FNP (median of 0.9 ppbv<sup>2</sup>). This could be caused by the combined effect of higher photolysis  
464 rates and reduced non-linear ozone chemistry.

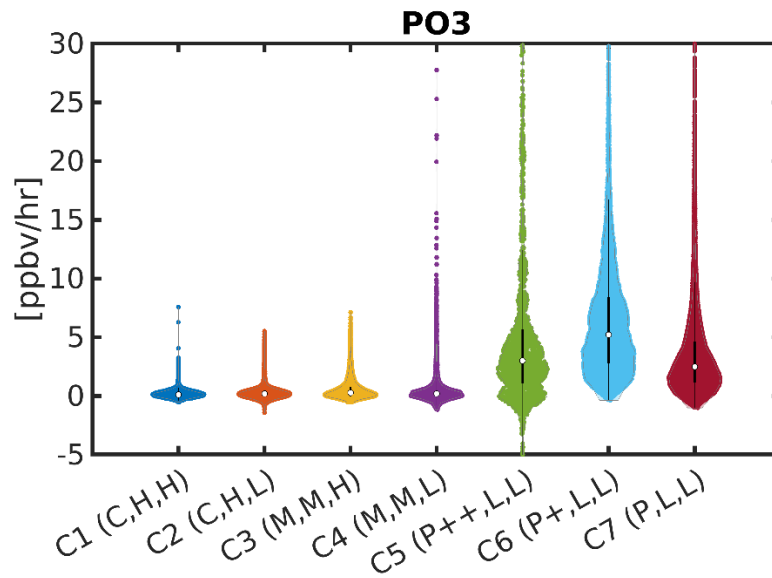
465 The analysis of aircraft data has revealed that the levels of HCHO and NO<sub>2</sub>, as well as the rates of  
466 jNO<sub>2</sub> and jO<sup>1</sup>D photolysis, play an important role in influencing PO<sub>3</sub>. Additionally, FNRs can offer insights  
467 into the sensitivity of PO<sub>3</sub> to its main precursors. These findings align with numerous other studies that  
468 have examined the factors driving PO<sub>3</sub> (e.g., Duncan and Chameides, 1998; Thornton et al., 2002; Kleiman  
469 et al., 2002; Gerasopoulos et al., 2006; Chatfield et al., 2010; Baylon et al., 2018; Wang et al., 2020; Souri  
470 et al., 2023). Consequently, our PO<sub>3</sub> estimates will incorporate HCHO, NO<sub>2</sub>, jNO<sub>2</sub>, jO<sup>1</sup>D, and FNR. While  
471 the cluster analysis did not definitively indicate whether meteorological conditions impact PO<sub>3</sub>, we will  
472 also include ambient temperature, water vapor, pressure, and SZA to determine if they provide any  
473 additional insights into PO<sub>3</sub> estimates.





474

475 **Figure 4.** The violin plots of six different parameters coming from the box model clustered into seven  
 476 distinct categories. Each cluster is described by three labels: air pollution levels (C: clean, M: moderately  
 477 clean, P: moderately polluted, P+: polluted, P++: extremely polluted), altitude (H: high, M: medium, L:  
 478 low), and SZA (H: high, L: low). The white dot is the median and the bars explain the 75<sup>th</sup> and 25<sup>th</sup>  
 479 percentiles. Both FNR and FNP are scaled using the logarithmic function to enable the simultaneous  
 480 visualization of low and high values within a single plot.



481

482 **Figure 5.** The corresponding violin plots of simulated  $\text{PO}_3$  for the seven clusters described in Figure 4.  
 483 The lowest  $\text{PO}_3$  is seen in remote regions (C-M) where ozone precursors are minimal. The highest  $\text{PO}_3$   
 484 does not happen in the most polluted region (P++) resulting from the non-linear ozone chemistry.

### 485 4.3. Estimates of $\text{PO}_3$

#### 486 4.3.1. LASSO coefficients

487 Armed with a procedure that finds the important features in a linear model (Section 3.1), we now  
 488 explore using LASSO for  $\text{PO}_3$  estimation. We make use of all data points generated by the observationally-  
 489 constrained box model from various atmospheric composition campaigns. Among the selected variables  
 490 shown in Figure 2, the LASSO algorithm assigns zero coefficients to SZA, pressure, temperature, and water  
 491 vapor, indicating that they offer less valuable information compared to other variables. This decision was  
 492 made by systematically adjusting the regularization factor within a 10-fold cross-validation framework to  
 493 identify the optimal factor that strikes a balance between solution variance and prediction bias. As a result,  
 494 the LASSO algorithm suggests that HCHO,  $\text{NO}_2$ ,  $\text{jNO}_2$ , and  $\text{JO}^1\text{D}$  contain sufficient information to  
 495 accurately predict  $\text{PO}_3$  for the most part.

496 Table 1 provides the intercepts and the corresponding coefficients for four different regions  
 497 separated by FNR. While we do not expect for a statistical model to fully single out the “cause and effect”  
 498 relationship between explanatory variables and the target, we note that it has some basic understanding of  
 499 ozone chemistry; the HCHO coefficients increase as moving towards smaller FNRs (i.e., more VOC-  
 500 sensitive). The same tendency is evident with respect to  $\text{NO}_2$  and larger FNRs (i.e., more  $\text{NO}_x$ -sensitive).  
 501 The negative coefficient of  $\text{NO}_2$  in regions having  $\text{FNR} \leq 1.5$ , implies some levels of non-linear feedback  
 502 embedded in this parameterization. Both  $\text{jNO}_2$  and  $\text{JO}^1\text{D}$  have positive coefficients throughout the chemical  
 503 conditions, suggesting that **higher** photolysis rates accelerate  $\text{PO}_3$ .  $\text{JO}^1\text{D}$  has a smaller effect than  $\text{jNO}_2$  on  
 504  $\text{PO}_3$  over remote regions ( $\text{FNR} \geq 3.5$ ) perhaps because of redundant information available compared to  $\text{jNO}_2$ .

505 **Table 1.** Calibrated coefficients derived from the LASSO estimator using seven atmospheric  
 506 composition aircraft campaigns.

Group	Criteria for FNR	Intercept	HCHO [ppbv]	$\text{NO}_2$ [ppbv]	$\text{jNO}_2 \times 10^3$ [ $\text{s}^{-1}$ ]	$\text{JO}^1\text{D} \times 10^6$ [ $\text{s}^{-1}$ ]
1	$\text{FNR} \leq 1.5$	-1.98	1.85	-0.14	0.12	0.09
2	$1.5 < \text{FNR} < 2.5$	-3.38	1.79	0.98	0.19	0.07
3	$2.5 < \text{FNR} < 3.5$	-3.27	1.07	3.48	0.21	0.03
4	$\text{FNR} \geq 3.5$	-1.63	0.41	6.54	0.11	0.01

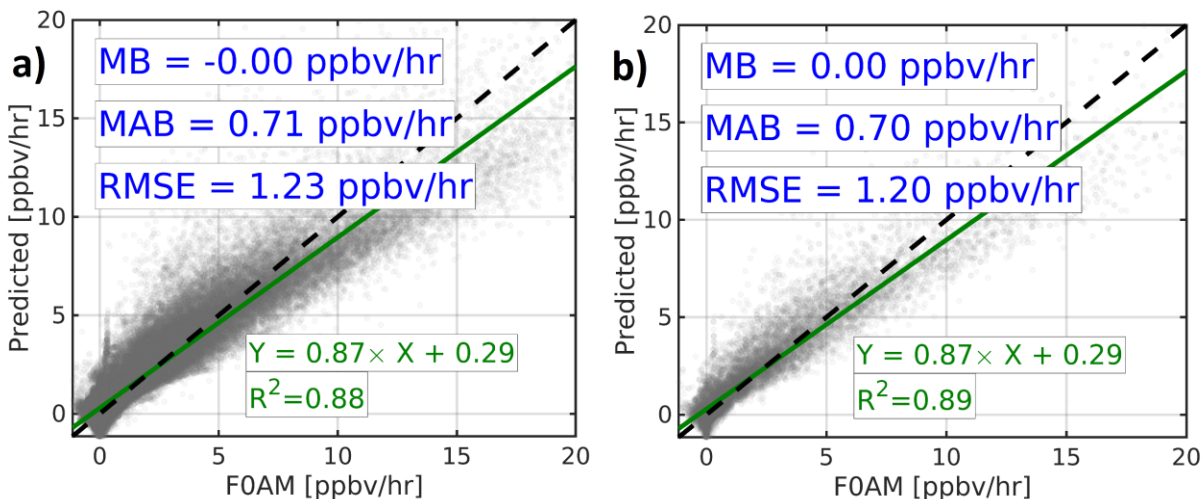
507

#### 508 4.3.2. Validation of $\text{PO}_3$ predictions

509 The validation of  $\text{PO}_3$  prediction against the box model results is performed in threefold with an  
 510 increasing stringency order: i) using all data points used in the LASSO algorithm, ii) by **randomly** dropping  
 511 data points, and iii) by dropping each air quality campaign from the LASSO estimation and using its data  
 512 as benchmark.

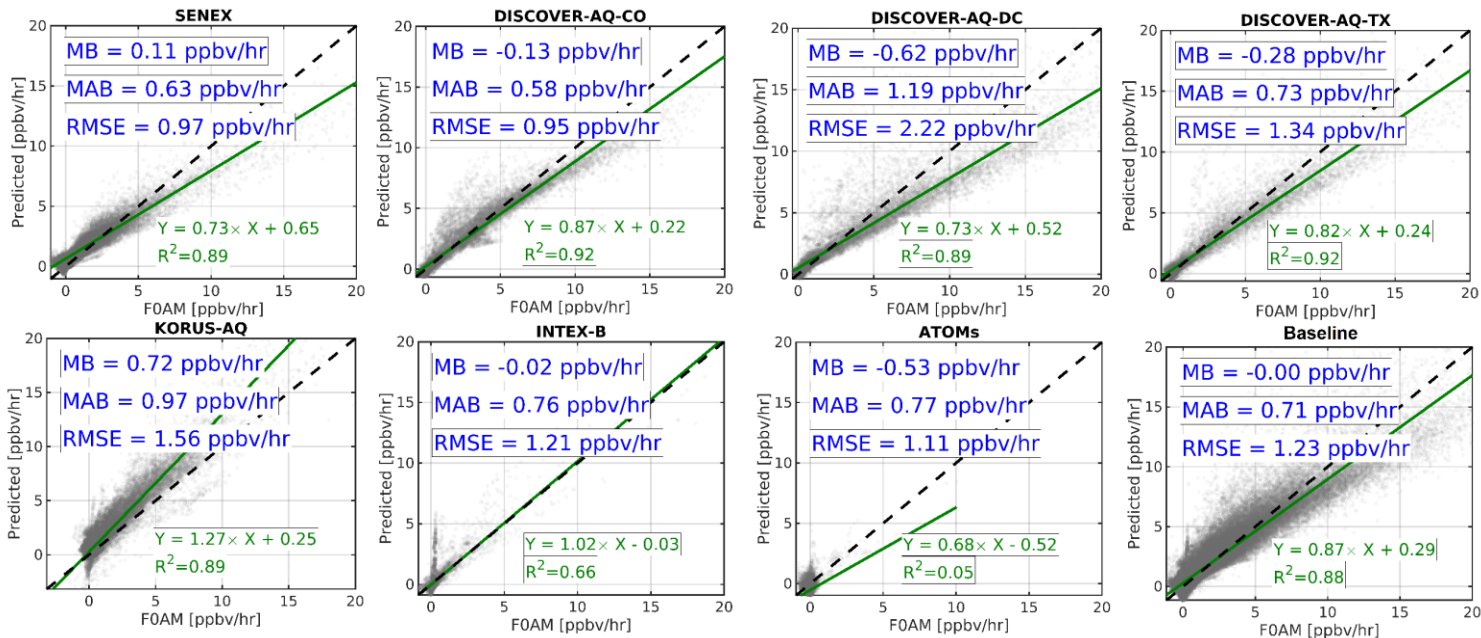
513 Figure 6a shows the scatterplot of predicted  $\text{PO}_3$  against the box model for all data points used to  
 514 estimate the coefficients described in Section 4.3.1. Despite the algorithm's simplicity, we can recreate more  
 515 than 88% of the variance in  $\text{PO}_3$  with negligible absolute bias. This has an important indication that our  
 516 scientific problem is not overly complex. There is less than 30% bias with respect to the mean absolute bias  
 517 of the prediction. The positive offset and a slope smaller than one indicate a mild underestimation  
 518 (overestimation) of  $\text{PO}_3$  in polluted (clean) regions. Figure 6b shows the same analysis for 20,000 randomly  
 519 chosen data points (~15% of the total) that we purposefully dropped from the LASSO estimation to gauge  
 520 if the predictor model can replicate numbers for points not used during the training. We find almost identical  
 521 statistics for these points, suggesting that the prediction stays robust for points outside the training data set.

522 However, the most stringent method is to drop each campaign data set entirely to understand where the  
523 prediction model struggles most.



524  
525 **Figure 6.** Scatterplots comparing observationally-constrained FOAM model  $PO_3$  and the predictions based  
526 on the proposed algorithm for (a) all data points and (b) 20,000 randomly-dropped data points as  
527 benchmarks. Despite the simplicity of the algorithm, we can reproduce a large variance in  $PO_3$  using only  
528 four explanatory variables.

529 Figure 7 shows several subplots pertaining to dropped campaigns from the analysis. Immediately  
530 evident is that our  $PO_3$  estimation has considerable skills at capturing  $PO_3$  for most polluted cases, including  
531 DISCOVER-AQs, KORUS-AQ, and SENEX without using their individual datasets. This provides  
532 convincing evidence about a high degree of generalizability of the predictor. However, the model has a  
533 reduction in performance in INTEX-B for  $PO_3 < 1$  ppbv/h. Moreover, the model prediction power is  
534 consistently poor for ATOMs where a significant fraction of airsheds were samples in pristine areas. We see  
535 such poor performance for  $PO_3 < 1$  ppbv/hr for other campaigns such as KORUS-AQ. Therefore, it is  
536 difficult to have confidence in the **predictive** power of the model in remote regions, which may be caused  
537 by the lack of inclusion of HOx, halogens, and H<sub>2</sub>O in the fit, as they can become an important sink for  
538 tropospheric ozone in those areas (Simpson et al., 2015). Nonetheless, while our predictive accuracy  
539 remains poor for this specific subset of the data, the practical utility and significance of this specific region  
540 (i.e., pristine areas) for air quality applications are notably limited. Given these results, we limit our  
541 predictions to  $PO_3 > 1$  ppbv/hr for the subsequent analyses.



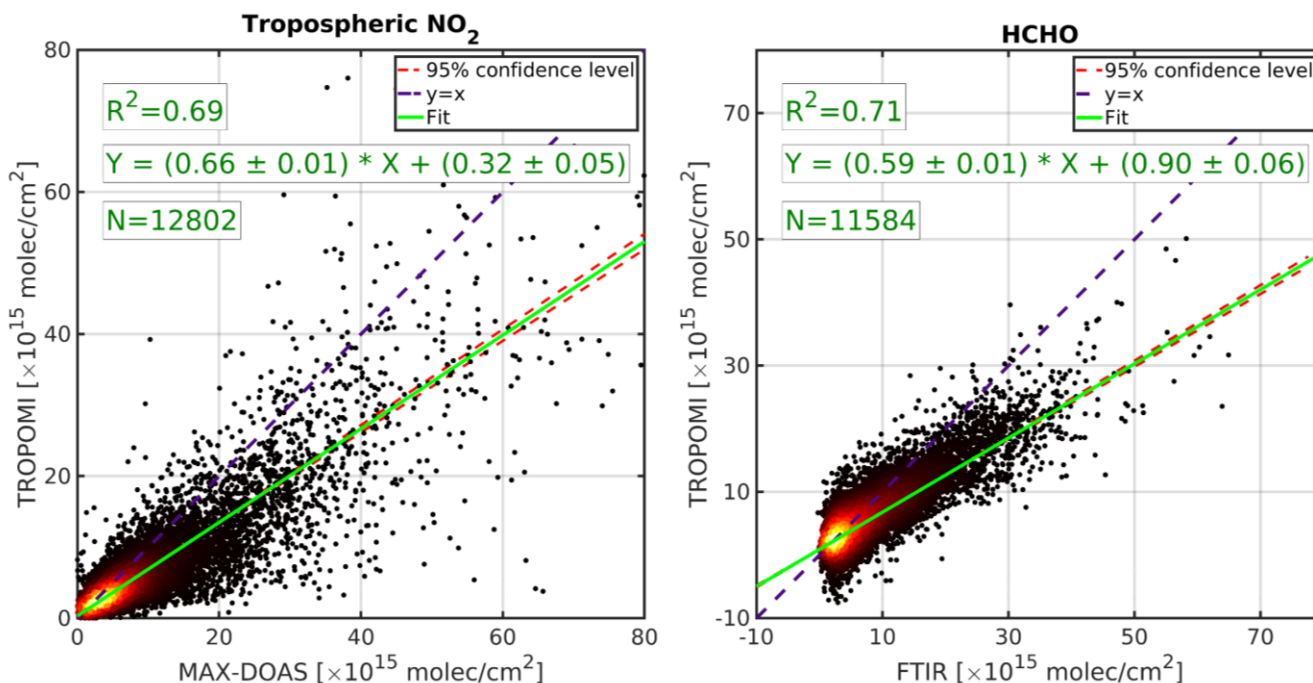
543 **Figure 7.** Same as Figure 6b, but each campaign is dropped from the LASSO estimation and subsequently  
 544 used as an independent benchmark. The designed algorithm has shown a high degree of skill at predicting  
 545  $\text{PO}_3$  in polluted regions; however, it performs poorly in pristine areas.

#### 546 4.3.3. TROPOMI $\text{NO}_2$ and HCHO validation

547 To build confidence in our quantitative application of TROPOMI data for  $\text{PO}_3$  estimates, we  
 548 validate the daily tropospheric  $\text{NO}_2$  and total HCHO columns against MAX-DOAS and FTIR observations  
 549 based upon the validation framework outlined in Vigouroux et al. (2020) and Verheolst et al. (2021). Both  
 550 paired datasets have been expanded to late 2023 showing a fuller picture of TROPOMI error  
 551 characterization compared to former studies. Figure 8 shows the comparison of daily TROPOMI, the  
 552 benchmarks and the optimal fit associated with their errors for the period of 2018-2023.

553 In the context of tropospheric  $\text{NO}_2$  comparison, we observe a slope smaller than one ( $\sim 0.66$ ) with  
 554 a positive offset ( $0.32 \times 10^{15} \text{ molec/cm}^2$ ). This tendency has been repeatedly documented in various studies  
 555 for various satellites or benchmarks (e.g., Griffin et al., 2019; Choi et al., 2020; Verhoelst et al. 2021; van  
 556 Geffen et al., 2022). A slope smaller than one, originating from unresolved systematic biases, implies that  
 557 TROPOMI is biased-low in polluted regions. A slight positive offset suggests that TROPOMI  $\text{NO}_2$  is  
 558 biased-high in remote regions. The errors of slope and the offset are relatively small, evidence of the  
 559 robustness of the optimal fit against the dataset variance. Nonetheless, we will incorporate them into Eqs 2  
 560 and 3 to take the adjustment error into consideration.

561 Despite the inherent difficulty in obtaining HCHO observations from the UV-Vis imagery  
 562 (González Abad et al., 2019), the HCHO comparison exhibits a good alignment with benchmarks. Like the  
 563 previous comparison, the slope is smaller than one ( $\sim 0.59$ ) and the offset is positive ( $\sim 0.9 \times 10^{15} \text{ molec/cm}^2$ )  
 564 agreeing within 10% with studies done by Vigouroux et al. (2020) and De Smedt et al. (2021).  
 565 Consequently, we will consider the fit errors and adjust all VCDs based on the slope and the offset obtained  
 566 from this comparison.



567

568 **Figure 8.** The comparison of TROPOMI tropospheric NO<sub>2</sub> and MAX-DOAS (left) and TROPOMI HCHO  
 569 and FTIR (right). The data points cover the period of 2018-2023. Both errors of in-situ measurements and  
 570 TROPOMI are considered in the fit. The data curation procedure has been discussed in Verhoelst et al.  
 571 (2021) and Vigouroux et al. (2020). The slope smaller than one suggests that both HCHO and NO<sub>2</sub> retrievals  
 572 are underestimated in polluted regions.

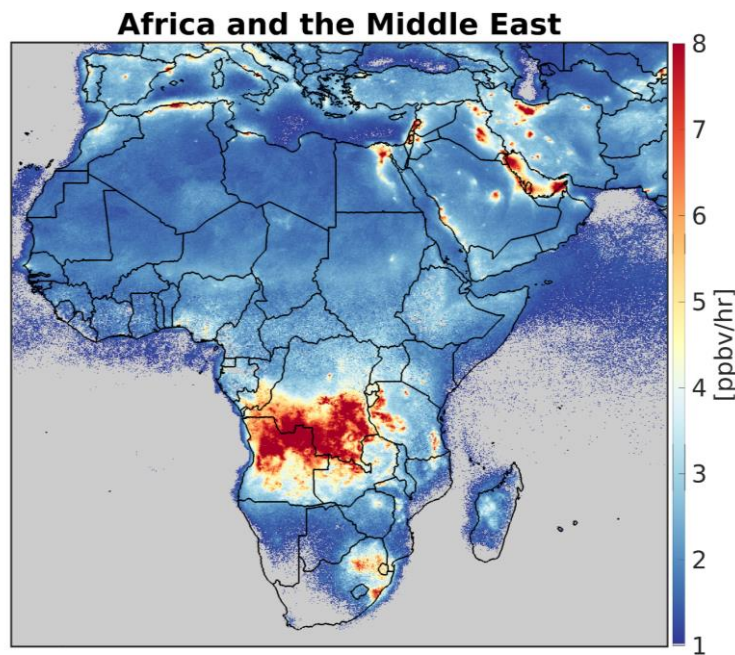
#### 573 4.3.4. Maps of PO<sub>3</sub> across various regions and qualitative description

574 Taking advantage of the wealth of bias-corrected TROPOMI observations, we present the first-ever  
 575 reported PO<sub>3</sub> maps at 0.1×0.1 degrees in the PBL in July 2019 across various geographic regions. Moreover,  
 576 because of the explicit nature of our algorithm, it is straightforward to break down the contributors of PO<sub>3</sub>  
 577 to gather insights into how each driver has shaped the distribution of PO<sub>3</sub>. Therefore, in addition to PO<sub>3</sub>  
 578 maps, we will show the magnitudes of various drivers of PO<sub>3</sub> including NO<sub>2</sub>, HCHO, and FNR  
 579 concentrations in the PBL region, the sum of scaled jO<sup>1</sup>D and jNO<sub>2</sub> values, along with their contributions  
 580 to PO<sub>3</sub>. It is worth noting that these maps are only a snapshot of PO<sub>3</sub> whose precursors can have large  
 581 interannual and interdecadal variability caused by meteorology, chemistry, and emissions. A discussion on  
 582 each region follows:

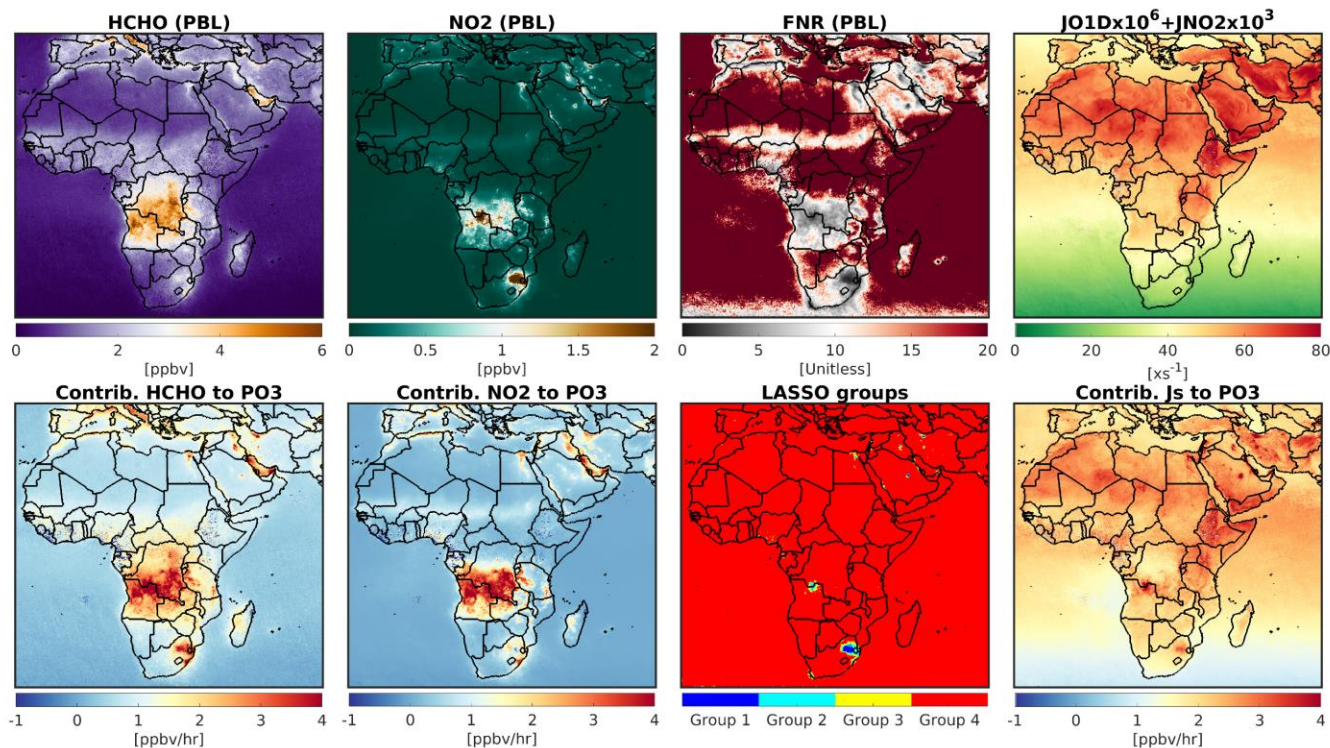
583 *Africa and the Middle East* – Figure 9 illustrates the **accelerated** rates of PO<sub>3</sub> over the region, particularly  
 584 concentrated over major cities such as Tehran (Iran), Cairo (Egypt), Riyadh (Saudi), Baghdad (Iraq), Algiers  
 585 (Algeria), and Johannesburg (South Africa). These urban areas consistently experience poor air quality  
 586 episodes (e.g., Chaichan et al., 2016; Belhout et al., 2018; Yousefian et al., 2020; Thompson et al., 2014;  
 587 Boraiy et al., 2023; Choi and Sourì et al. 2015a). The biomass burning activities in Africa (see Figure 1 in  
 588 Roberts et al., 2009) significantly contribute to the high rates of PO<sub>3</sub>. Moreover, we see accelerated PO<sub>3</sub>  
 589 over the Persian Gulf, a region housing oil and gas production facilities, leading to high PO<sub>3</sub> in the region  
 590 (Lelieveld et al., 2009; Choi and Sourì et al. 2015a). Figure 10 shows NO<sub>2</sub> and HCHO concentrations are  
 591 highly correlated in the Middle East ( $r=0.82$ ) due to co-emitted NO<sub>x</sub> and VOC emissions, predominantly  
 592 from anthropogenic sources. Over the whole region, HCHO and NO<sub>2</sub> concentrations are only moderately  
 593 correlated ( $r=0.61$ ). This is because there is strong spatial heterogeneity associated with NO<sub>x</sub> and VOC  
 594 emissions over Africa that are not spatially correlated. One possible explanation for this could be the  
 595 emission dependence on the type of fire combustion in Africa (van der Velde et al., 2021) and the location



596 of biogenic isoprene emissions (Marais et al., 2014). For the most part, FNRs tend to fall in ranges above  
597 >3.5 (LASSO group 4, highly NO<sub>x</sub>-sensitive). However, lower FNRs are prevalent in the core of cities due  
598 to elevated NO<sub>x</sub> emissions. The contributions of HCHO to PO<sub>3</sub> occur predominantly over areas with low  
599 FNRs. These results suggest that NO<sub>x</sub> emissions dictate the location of maximum VOC contributions to  
600 PO<sub>3</sub>. The contribution of NO<sub>2</sub> to PO<sub>3</sub> behaves non-linearly with negative values at the core of cities such as  
601 Johannesburg and Tehran (Figure S2). Photolysis rates are high over low SZA and bright surface albedo  
602 (i.e., arid land). Accordingly, photolysis rates exhibit a latitudinal gradient in response to changes in SZA.  
603 Greater contributions of photolysis rates to PO<sub>3</sub> are observed in areas with low FNRs, as determined by the  
604 LASSO estimator (Table 1).



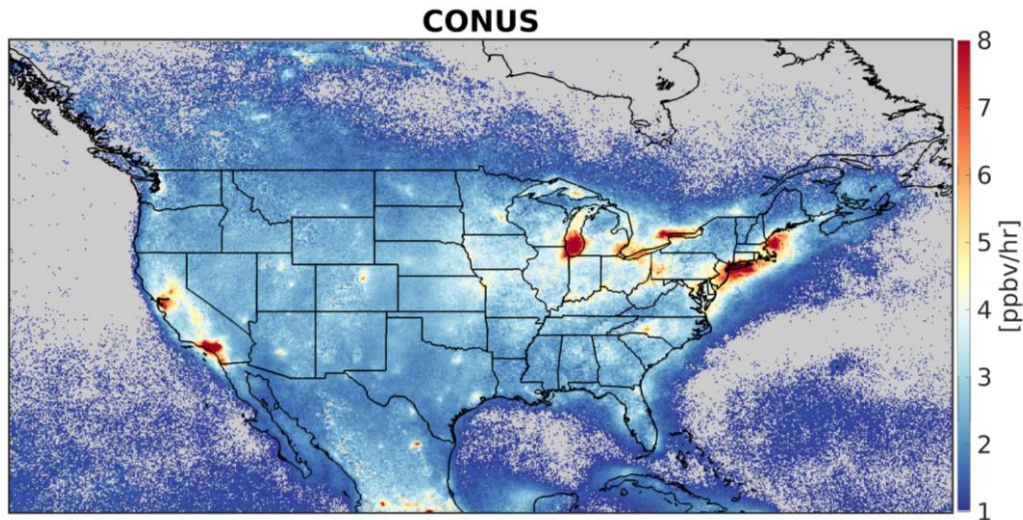
605  
606 **Figure 9.** The spatial distribution of PO<sub>3</sub> within the PBL region averaged over July 2019 in Africa and the  
607 Middle East. PO<sub>3</sub><1 ppbv/hr is masked due to the algorithm deficiencies. Accelerated PO<sub>3</sub> can be seen over  
608 major cities and biomass burning activities in Africa.



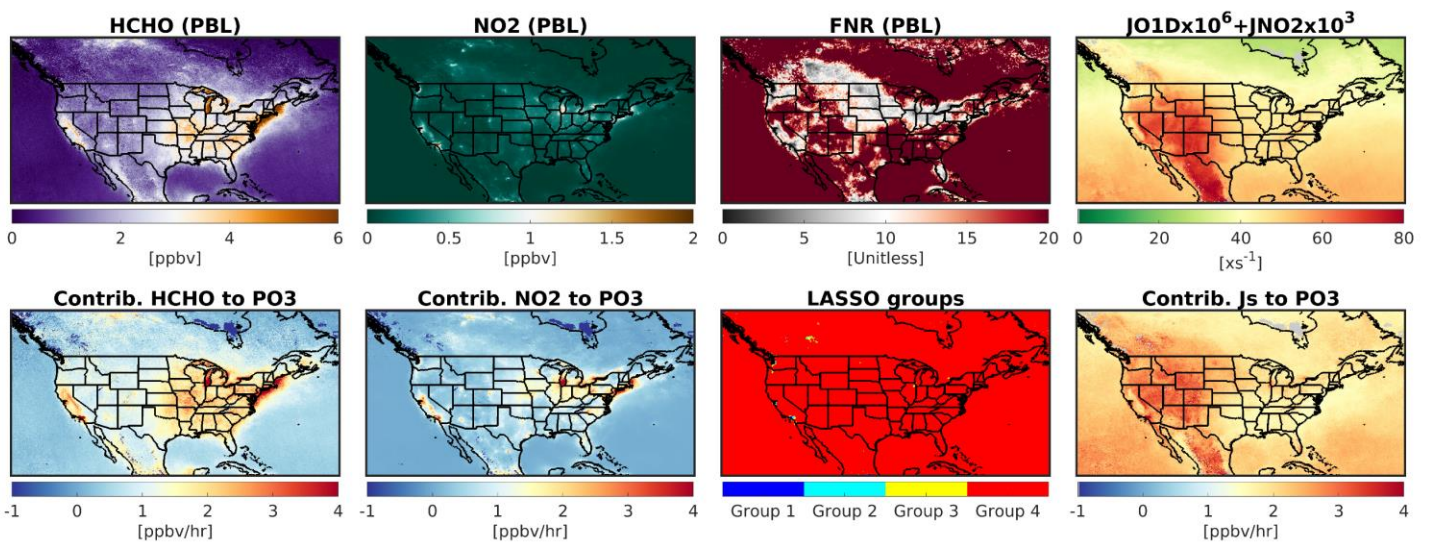
609  
 610 **Figure 10.** (first row) PBL concentrations of HCHO, NO<sub>2</sub>, FNR and sum of scaled jO<sup>1</sup>D and jNO<sub>2</sub> derived  
 611 from TROPOMI and models in July 2019; (second row) the contributions of HCHO, NO<sub>2</sub>, and photolysis  
 612 rates to PO<sub>3</sub>, along with the defined LASSO ozone production sensitivity regimes for PO<sub>3</sub> estimates.

613 *Contiguous United States (CONUS)* – New York City, Los Angeles (LA), the San Francisco Bay area, and  
 614 Lake Michigan areas all experience accelerated PO<sub>3</sub> in July 2019, as shown in Figure 11. All the regions  
 615 fall into non-attainment regions (marginal to extreme) with respect to ozone standards and have been  
 616 immensely studied (Wu et al., 2024; Kim et al., 2022; Stainer et al., 2021). **A robust relationship between**  
 617 **PO<sub>3</sub> and ozone concentrations can only be established by factoring in physical processes such as horizontal**  
 618 **and vertical transport, dry deposition rates, and background values. In regions with high background ozone**  
 619 **concentrations, for example in mountainous areas, even a moderate level of PO<sub>3</sub> can elevate ozone**  
 620 **concentration to unhealthy levels. Conversely, if there is a strong correlation between PO<sub>3</sub> and frequent**  
 621 **ozone exceedances, such as those observed in the mentioned U.S. cities, it indicates that locally produced**  
 622 **ozone through chemical reactions is the primary factor contributing to those events. Except for LA, the vast**  
 623 **majority of CONUS fall into large FNRs (>3.5), meaning NO<sub>2</sub> levels largely shape the spatial distribution**  
 624 **of PO<sub>3</sub> (Figure 12). HCHO levels are found to be relatively large over LA, causing PO<sub>3</sub> to increase due to**  
 625 **its greater sensitivity to VOCs. In addition to high levels of HCHO and NO<sub>2</sub> in several Californian regions,**  
 626 **accelerated photochemistry caused by the bright surface albedo enhances PO<sub>3</sub>.**





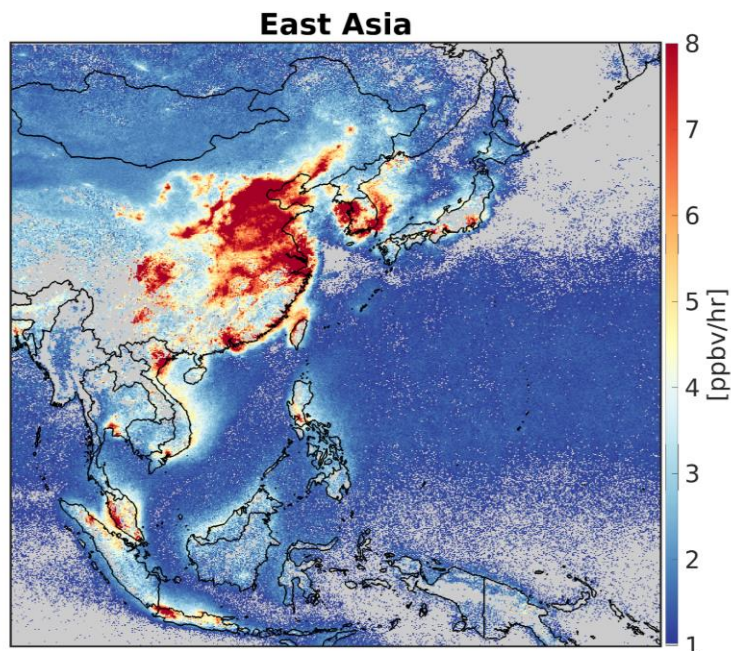
627  
 628 **Figure 11.** Same as Figure 9 but for CONUS. Elevated PO<sub>3</sub> prevails over various areas such as New York  
 629 City, Los Angeles, San Francisco Bay area, and Lake Michigan.



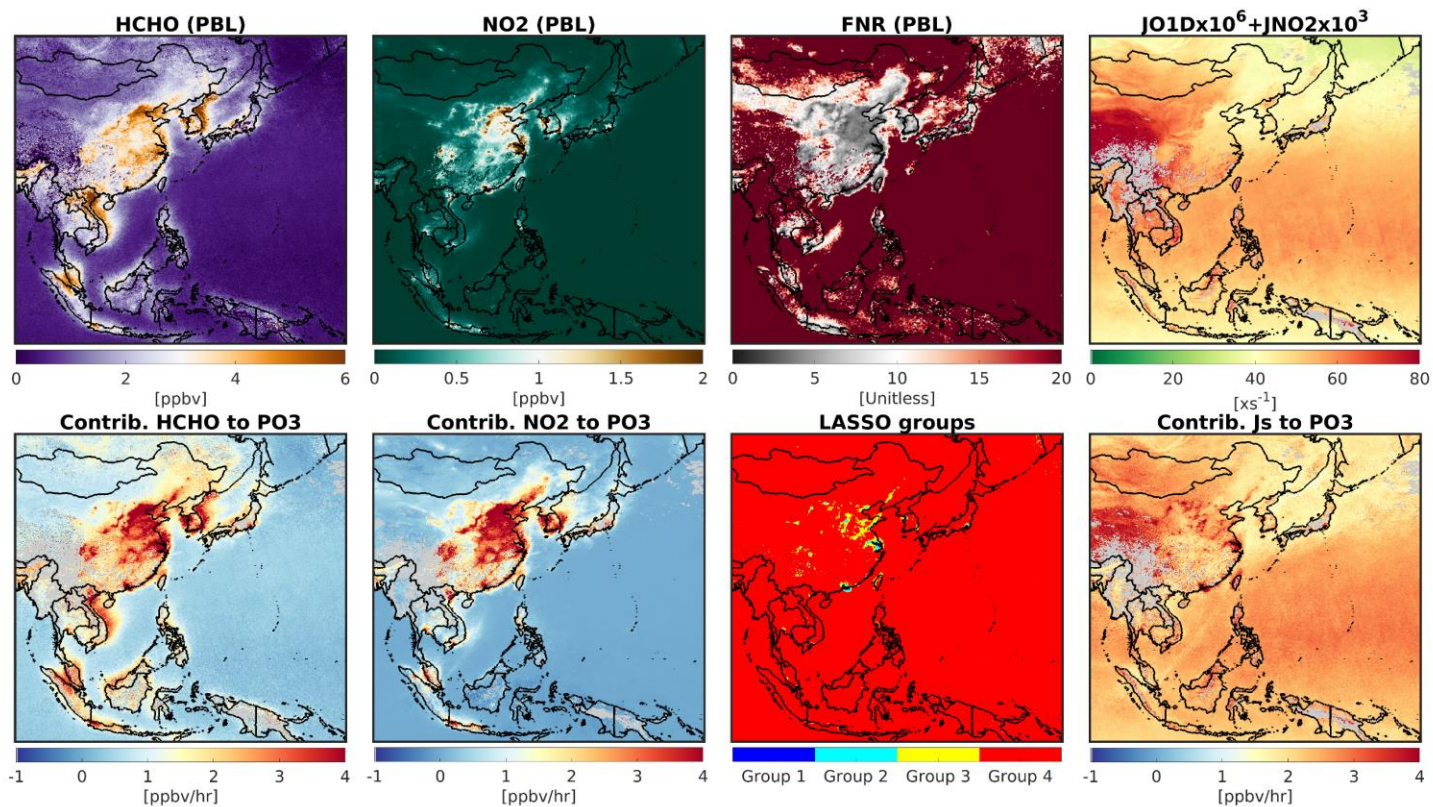
631 **Figure 12.** Same as Figure 10 but for CONUS.

632 *East and Southeast Asia* – Figure 13 shows extremely accelerated PO<sub>3</sub> values over East Asia, particularly  
 633 over North China Plain, Yangtze River Delta, Pearl River Delta, and Seoul. These regions have experienced  
 634 severely degraded air quality with respect to ozone (Souri et al., 2020a,b; Li et al., 2019; Colombi et al.,  
 635 2023; Schroeder et al., 2020; Wang et al., 2017; Zhang et al., 2007). In southeast Asia, Hanoi (Vietnam),  
 636 Kuala Lumpur (Malaysia), and Jakarta (Indonesia), undergoing heightened PO<sub>3</sub> as well, have received less  
 637 attention in literature (Ahamad et al., 2020; Kusumaningtyas et al., 2024; Sakamoto et al., 2018). Figure 14  
 638 suggests that the chemical condition of many regions in China and South Korea, falling within the  
 639 transitional regimes (LASSO group 2 and 3, 1.5 < FNR < 3.5), has made them susceptible to high PO<sub>3</sub> levels  
 640 due to concurrent high concentrations of HCHO and NO<sub>2</sub>. Moreover, photochemistry appears to be active  
 641 throughout the region.



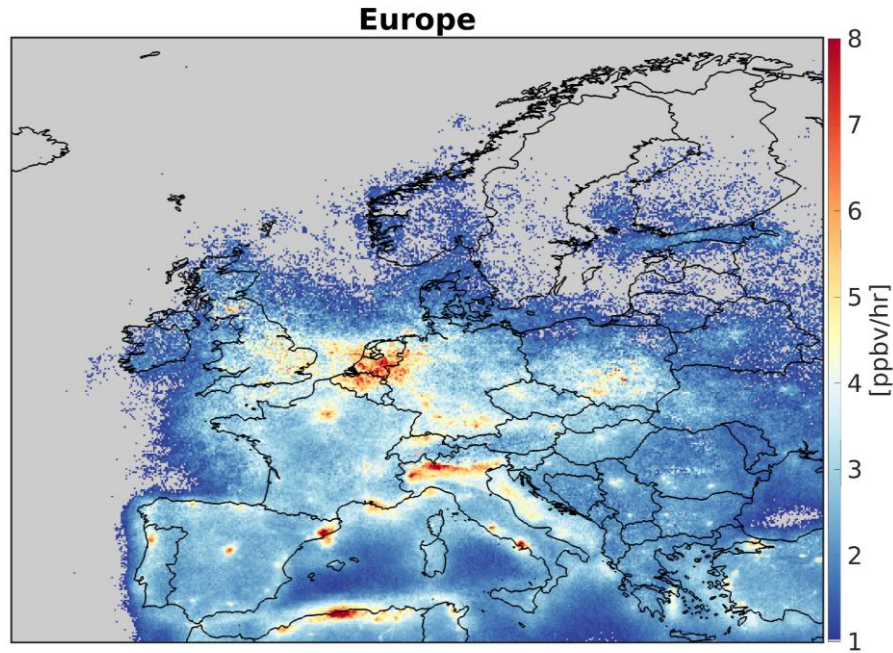


642  
 643 **Figure 13.** Same as Figure 9 but for east and southeast Asia. Because of heightened amount of  
 644 photochemistry,  $\text{NO}_2$ , and HCHO, we observe accelerated  $\text{PO}_3$  throughout the majority of the cities in East  
 645 and Southeast Asia.



647 **Figure 14.** Same as Figure 10 but for east and southeast Asia.

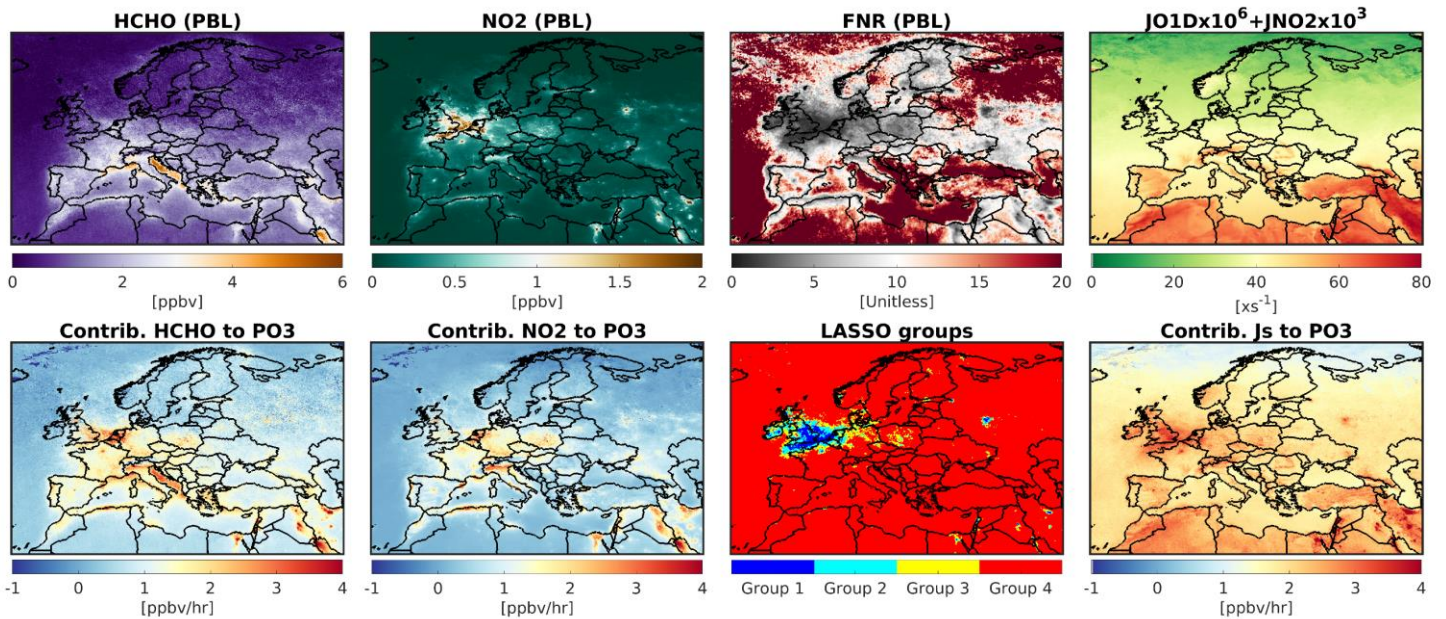
648 *Europe* – Figure 15 reveals high  $\text{PO}_3$  over Benelux (Belgium, The Netherlands, and Luxembourg), Po  
649 Valley (Italy), and several major cities such as Barcelona (Spain) and Rome (Italy). Benelux has the largest  
650 hotspot of  $\text{PO}_3$  in the region (e.g., Zara et al., 2021). A significant portion of England, Benelux, fall into  
651 VOC-sensitive, or the transitional regime ( $\text{FNR} < 2.5$ ) shown in Figure 16. Because of diminished  
652 photochemistry in these high latitude regions, we do not see significant PBL concentrations of HCHO in  
653 order for  $\text{PO}_3$  to be as high as the previous areas; moreover, the non-linear  $\text{NO}_x$  feedback has led to negative  
654 contributions of  $\text{NO}_2$  to  $\text{PO}_3$  in several cities such as London. In general, low photolysis rates compared to  
655 the previous regions have made most of Europe less prone to elevated  $\text{PO}_3$ .



656

657 **Figure 15.** Same as Figure 9 but for Europe. Because of reduced photochemistry,  $\text{PO}_3$  values tend to be  
658 smaller than the previous cases. Benelux has experienced the highest  $\text{PO}_3$  in this region.





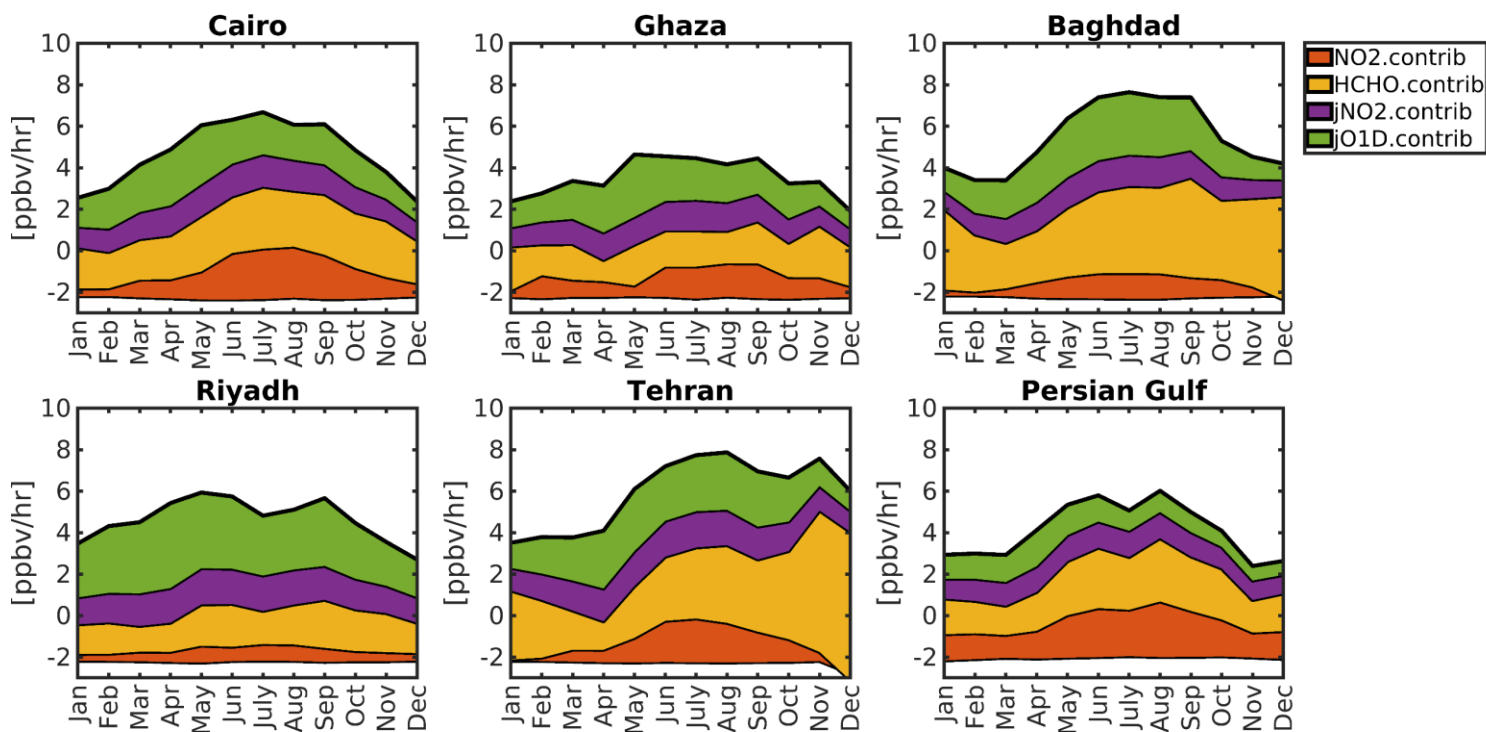
€

660 **Figure 16.** Same as Figure 10 but for Europe.

661 *4.3.5. Seasonality of PO<sub>3</sub> over the Middle East*

662 It is attractive to study the seasonal variations in the contributors to PO<sub>3</sub> over several major cities  
 663 because the PO<sub>3</sub> drivers' seasonality can vary from location to location. We decide to focus on several  
 664 Middle Eastern countries that have experienced rapid growth and degraded air quality: Cairo (Egypt),  
 665 Ghaza (Palestine), Baghdad (Iraq), Riyadh (Saudi Arabia), Tehran (Iran), and the Persian Gulf region. We  
 666 illustrate the seasonality of four major contributors to PO<sub>3</sub> including NO<sub>2</sub>, HCHO, jNO<sub>2</sub>, and jO<sup>1</sup>D in 2019  
 667 in Figure 17.

668 The levels of HCHO (a proxy for VOCs) consistently have the greatest impact on PO<sub>3</sub> throughout  
 669 the year in these regions. Specifically, both Baghdad and Tehran experience high levels of HCHO even  
 670 during colder months, which can be observed using TROPOMI. This suggests that regulations targeting the  
 671 reduction of man-made VOC emissions should be prioritized in this region. PO<sub>3</sub> levels over Cairo, Gaza,  
 672 Baghdad, and the Persian Gulf peak during summertime, while Tehran experiences a comparable peak in  
 673 the autumn due to increased VOC emissions. Additionally, we notice a decrease in PO<sub>3</sub> levels over the  
 674 Persian Gulf and Riyadh in July, possibly due to a decline in HCHO contributions caused by meteorological  
 675 factors. Even though NO<sub>2</sub> concentrations decline in summertime due to shorter lifetime against OH, the  
 676 higher amount of HCHO makes PO<sub>3</sub> more sensitive to NO<sub>2</sub> in this season. Ghaza shows the least seasonal  
 677 variation among these regions, likely due to consistently active photochemistry throughout the year.



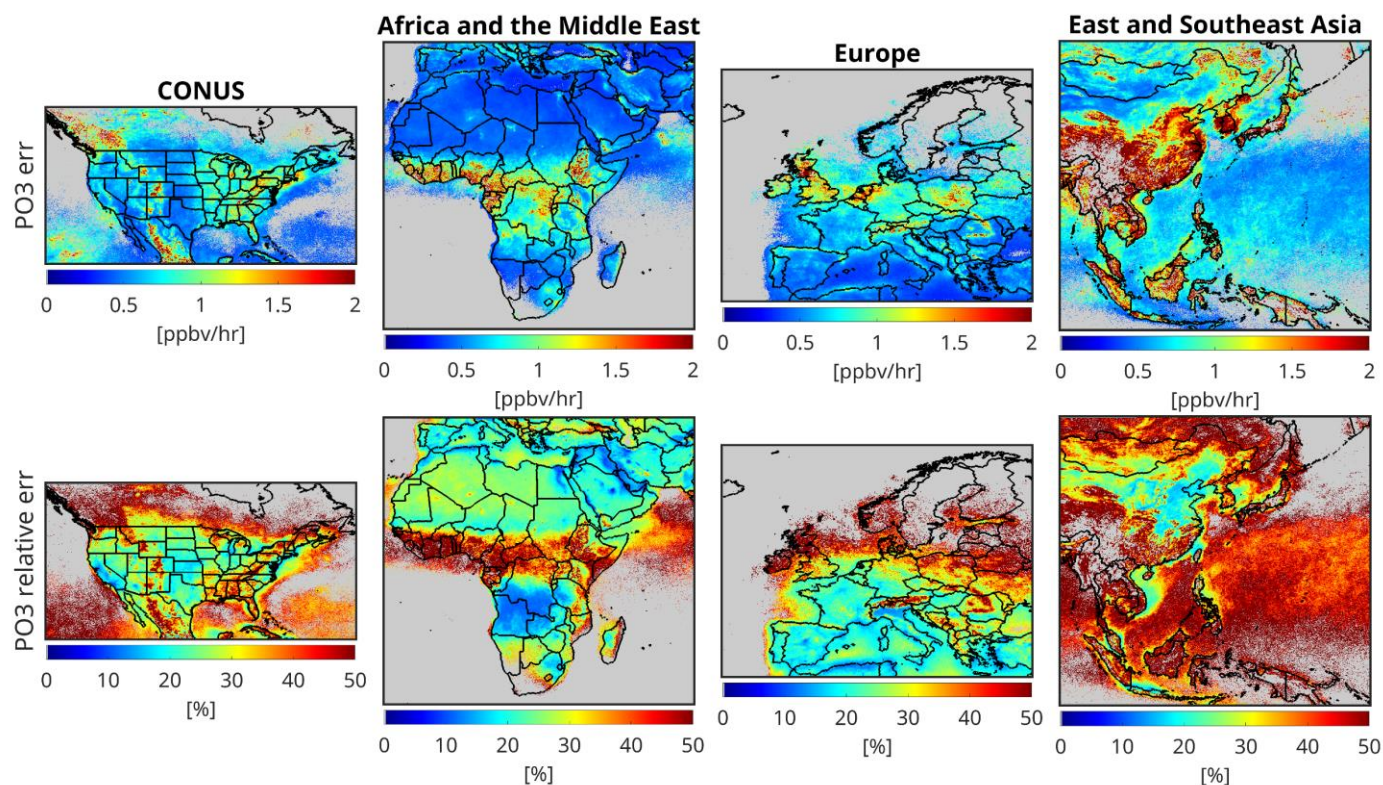
679 **Figure 17.** The contributions of NO<sub>2</sub>, HCHO, jNO<sub>2</sub>, and jO<sup>1</sup>D to the PBL PO<sub>3</sub> for several major regions in  
 680 the Middle East. **These estimates are based on the proposed algorithm integrating TROPOMI, ground-based**  
 681 **remote sensing, and atmospheric models, to estimate PO<sub>3</sub> based upon a statistical approach.** PO<sub>3</sub> tends to  
 682 spike around the summer due to increased HCHO, higher sensitivity of PO<sub>3</sub> to NO<sub>x</sub>, and enhanced  
 683 photochemistry. However, Tehran shows a second peak in autumn due to unusual high values of HCHO.

684 *4.3.6. The effect of satellite errors on PO<sub>3</sub>*

685 Satellite retrieval errors have been identified as the primary obstacle to achieving a robust  
 686 understanding of ozone chemistry using HCHO and NO<sub>2</sub> data (Souri et al., 2023; Johnson et al., 2023);  
 687 therefore, generating uncertainty maps is crucial for informing the scientific community about the  
 688 credibility of our PO<sub>3</sub> estimates. In this study, we utilize the equations outlined in Section 2.2.1 to propagate  
 689 the errors of HCHO and NO<sub>2</sub> retrievals to the final PO<sub>3</sub> estimates. We achieve this by recalculating the PO<sub>3</sub>  
 690 value for a given pixel 10,000 times, with each recalculation based on a sample drawn from a normal  
 691 distribution with a standard deviation equal to the satellite total error. The standard deviation of these  
 692 samples offers a good approximation of the impact of satellite errors on PO<sub>3</sub> estimates.

693 Figure 18 illustrates the maps of PO<sub>3</sub> absolute and relative errors over the targeted regions in the  
 694 course of the month of July. The errors of PO<sub>3</sub> estimates tend to be high (> 50%) in remote regions where  
 695 the trace gas signals are small. However, the PO<sub>3</sub> errors are within 10-20% in polluted regions where the  
 696 signals are larger. Currently, the absence of absolute measurements of PO<sub>3</sub> at this vast spatial coverage  
 697 makes it challenging to judge the severity of these errors for PO<sub>3</sub> applications. Nonetheless, any application  
 698 based on this product should be recalculated within the reported errors through a Monte-Carlo to gauge the  
 699 significance of the outcome.





701 **Figure 18.** The influence of the satellite errors on  $\text{PO}_3$  estimates (absolute and relative) over four major  
 702 regions tackled in this work. The errors are based on monthly-averaged TROPOMI errors. The errors tend  
 703 to be mild over polluted regions (10-20%) but they can exceed above 50% over pristine ones.

## 704 5. Conclusion

705 Providing data-driven and integrated maps of ozone production rates ( $\text{PO}_3$ ) using a synergy of  
 706 satellite retrievals, ground-based remote sensing, and atmospheric models enabled us to generate the first  
 707 satellite-informed product of this kind, offering extensive spatial coverage with important applications in  
 708 atmospheric chemistry. These data have indeed extended the use of formaldehyde (HCHO) over nitrogen  
 709 dioxide ( $\text{NO}_2$ ) ratios (FNR) beyond their current role. Through this product, we can shed light on the effects  
 710 of emission regulations, wildfires, widespread lockdown, wars, and economic recessions on  $\text{PO}_3$  levels.  
 711 Furthermore, given the long-term records of satellite observations (e.g., OMI since 2005 and TROPOMI  
 712 since 2018), this product can inform emission regulators about locally-produced ozone hotspots, and  
 713 ultimately, enhance our understanding of the spatiotemporal variability of ozone formation for over two  
 714 decades.

715 In this study, we generated  $\text{PO}_3$  maps within the planetary boundary layer (PBL), constrained by  
 716 bias-corrected TROPospheric Monitoring Instrument (TROPOMI) observations, using a piecewise  
 717 regularized regression model. This model was calibrated using a blend of data from a comprehensive suite  
 718 of aircraft observations and a well-characterized box model. These maps, produced for various regions,  
 719 allowed us to identify hotspots of locally-produced ozone pollution with unprecedented resolution. Our  
 720 findings indicated that numerous urban areas in the Middle East, East Asia, and Southeast Asia exhibit  
 721 accelerated  $\text{PO}_3$  rates ( $>8$  ppbv/hr), attributed to high levels of anthropogenic nitrogen oxides ( $\text{NO}_x = \text{NO}$   
 722 +  $\text{NO}_2$ ), volatile organic compounds (VOCs), and active photochemistry. In contrast, such elevated  $\text{PO}_3$   
 723 levels were less prevalent in the United States and Europe, with exceptions including Los Angeles, New

724 York City, and the entire region of the Benelux. Additionally, biomass burning activities in Africa  
725 contributed to high PO<sub>3</sub> rates across extensive areas. Seasonality of PO<sub>3</sub> peaked around the summer for  
726 several regions in the Middle East because of active photochemistry and concurrent large HCHO and NO<sub>2</sub>  
727 levels; however, Tehran experienced elevated PO<sub>3</sub> in the autumn due to large HCHO values possibly  
728 produced from anthropogenic emissions.

729 The production of these maps relied heavily on a robust training dataset. To this end, we  
730 incorporated an extensive array of aircraft observations from multiple atmospheric composition campaigns,  
731 including DISCOVER-AQ, KORUS-AQ, INTEX-B, ATOM, and SENEX, into the Framework for 0-D  
732 Atmospheric Modeling (F0AM) photochemical box model. The box model demonstrated a high level of  
733 correspondence ( $R^2 > 0.6$ , with minimal biases) between several unconstrained compounds (e.g., HCHO,  
734 OH, HO<sub>2</sub>, PAN, NO, and NO<sub>2</sub>) and their observed counterparts, indicating its effectiveness in understanding  
735 local ozone chemistry. Utilizing a classification algorithm applied to the data obtained from the constrained  
736 box model, we identified HCHO, NO<sub>2</sub>, their ratio (known as FNR), photolysis rates, and, to some extent,  
737 meteorological factors as good candidates for reproducing PO<sub>3</sub> variability and magnitudes.

738 Subsequently, we employed a piecewise linear model known as LASSO, which is capable of  
739 feature selection by eliminating unimportant inputs, to parameterize PO<sub>3</sub>. A key component of this  
740 parameterization was the use of FNR to empirically linearize the non-linear ozone chemistry. The LASSO  
741 algorithm indicated that more than 88% of the variance in PO<sub>3</sub> could be reproduced with low bias using  
742 only five parameters: FNR, HCHO, NO<sub>2</sub>, jNO<sub>2</sub> (photolysis rates for NO<sub>2</sub> + hv), and jO<sup>1</sup>D (photolysis rates  
743 for O<sub>3</sub> + hv). This parameterization demonstrated remarkable performance for the majority of air parcels  
744 collected in moderately to extremely polluted regions (PO<sub>3</sub> > 1 ppbv/hr). However, it performed poorly in  
745 pristine regions due to the exclusion of certain ozone loss pathways, such as HO<sub>x</sub> (OH+HO<sub>2</sub>), which are  
746 more challenging to predict.

747 Fortunately, TROPOMI provided critical data to enhance the representation of FNR, HCHO, NO<sub>2</sub>,  
748 jNO<sub>2</sub>, and jO<sup>1</sup>D. We utilized TROPOMI's viewing geometry, UV surface albedo, and total ozone overhead  
749 from a model to predict jNO<sub>2</sub> and jO<sup>1</sup>D using look-up tables derived from NCAR's TUV model. To convert  
750 TROPOMI tropospheric NO<sub>2</sub> and HCHO columns to their PBL mixing ratios, we employed the  
751 MERRA2GMI global transport model, extensively used in various studies. However, the coarse resolution  
752 of this model might have introduced underrepresentation issues, which could be mitigated by using higher  
753 spatial resolution models in future research.

754 To address the biases associated with TROPOMI observations, we updated comparisons from  
755 Verhoelst et al. (2021) and Vigouroux et al. (2020) with a larger dataset of paired TROPOMI and  
756 FTIR/MAX-DOAS measurements. TROPOMI retrievals significantly underestimated HCHO and NO<sub>2</sub>  
757 magnitudes in polluted regions (slope ~0.6 - 0.7) and moderately overestimated them in pristine areas.  
758 These biases were corrected using regression lines, enabling a relatively unbiased application of the data.

759 To build confidence in our product, we propagated TROPOMI HCHO and NO<sub>2</sub> errors to PO<sub>3</sub>  
760 estimates using a Monte Carlo approach. Results indicated that PO<sub>3</sub> estimates were uncertain (>50%) in  
761 clean regions due to a low trace gas signal in TROPOMI retrievals. However, in polluted regions, the errors  
762 were more moderate (10-20%) due to the stronger signal.

763 Over the years, extensive efforts have been devoted to measuring various critical atmospheric  
764 compounds globally, developing robust atmospheric models, and enhancing satellite retrievals along with  
765 their benchmarks. These advancements have enabled us to estimate PO<sub>3</sub> maps within the PBL. Nonetheless,  
766 it is crucial to acknowledge some limitations of our work, many of which are the focus of ongoing research  
767 within our team:



768 i) The direct measurement of PO<sub>3</sub> using specialized instruments (Cazorla and Brune, 2010;  
769 Sadanaga et al., 2017; Sklaveniti et al., 2018) is lacking in most atmospheric composition datasets, limiting  
770 our ability to fully understand the effects of assumptions (such as the exclusion of heterogeneous chemistry)  
771 made in the box model on PO<sub>3</sub>.

772 ii) There is potential for improvement in the parameterization process by employing more  
773 sophisticated algorithms, such as neural networks, which could increase the variance explained in the  
774 predicted PO<sub>3</sub>.

775 iii) The conversion of satellite column data to PBL mixing ratios requires error characterization  
776 and the use of finer-resolution models that are comparable in size to the PO<sub>3</sub> grid boxes.

777 iv) Partially cloudy pixels and aerosols can affect photolysis rates, which should be considered in  
778 future parameterization efforts.

779 It is important to recognize that PO<sub>3</sub> maps are just one piece of the puzzle when it comes to  
780 determining ozone concentrations. Several studies have indicated that accurately representing surface ozone  
781 is challenging due to difficulties in representing background ozone, transport, and dry deposition rates.  
782 Therefore, we advise against directly linking high PO<sub>3</sub> rates from our product to increased unhealthy ozone  
783 exposure. However, our product does provide indications as to whether heightened ozone concentrations  
784 are associated with chemistry contributions as opposed to other processes (e.g., meteorology or dry  
785 deposition rates). Further investigation using additional tools/data is necessary to gather a full picture of  
786 these processes.

787 Despite these limitations, our novel product offers an asset to the atmospheric science community.  
788 It provides a more comprehensive understanding of the complexities associated with spatiotemporal  
789 variability associated with the non-linear ozone chemistry at a large domain and enhances confidence in  
790 high-resolution maps of **chemically**-produced ozone hotspots.

## 791 **Financial Support**

792 This study is funded by NASA's ACOMAP/Aura project (grant no. 80NSSC23K1250). The measurements  
793 at Paramaribo have been supported by the BMBF (German Ministry of Education and Research) in project  
794 ROMIC-II's subproject TroStra (01LG1904A). The NDACC FTIR stations Bremen, Garmisch, Izaña, Ny-  
795 Ålesund, Paramaribo, and Karlsruhe have been supported by the German Bundesministerium für Wirtschaft  
796 und Energie (BMWi) via DLR5 under grants 50EE1711A, B, and D. The measurements and data analysis  
797 at Bremen are supported by the Senate of Bremen. The NCAR FTS observation programs at Thule, GR,  
798 Boulder, CO, and Mauna Loa, HI, are supported under contract by the National Aeronautics and Space  
799 Administration (NASA). The National Center for Atmospheric Research is sponsored by the National  
800 Science Foundation. The Thule effort is also supported by the NSF Office of Polar Programs (OPP).  
801 Operations at the Rikubetsu and Tsukuba FTIR sites are supported in part by the GOSAT series project. The  
802 Paris TCCON site has received funding from Sorbonne Université, the French research center CNRS, and  
803 the French space agency CNES. The Jungfraujoch FTIR data are primarily available thanks to the support  
804 provided by the F.R.S. FNRS (Brussels), the GAW-CH program of MeteoSwiss (Zürich), and the HFSJG.ch  
805 Foundation (Bern). IUP-Bremen ground-based measurements are funded by DLR-Bonn and received  
806 through project 50EE1709A. KNMI ground-based measurements in De Bilt and Cabauw are partly  
807 supported by the Ruisdael Observatory project, Dutch Research Council (NWO) contract 184.034.015, by  
808 the Netherlands Space Office (NSO) for Sentinel-5p/TROPOMI validation, and by ESA via the EU CAMS  
809 project.

## 810 **Data Availability**

811 TROPOMI satellite data are derived from copernicus Sentinel-5P (processed by ESA), 2021, TROPOMI  
812 Level 2 Nitrogen Dioxide total column products. Version 02. European Space Agency.  
813 <https://doi.org/10.5270/S5P-9bnp8q8>, and copernicus Sentinel-5P (processed by ESA), 2020, TROPOMI  
814 Level 2 Formaldehyde Total Column products. Version 02. European Space Agency.  
815 <https://doi.org/10.5270/S5P-vg1i7t0>. The FTIR and MAX-DOAS observations were partly obtained from  
816 the Network for the Detection of Atmospheric Composition Change (NDACC) and are available through  
817 the NDACC website at <http://www.ndacc.org>. The box model can be obtained from  
818 <https://github.com/AirChem/F0AM> (last access: 10 Nov, 2024). The TROPOMI UV DLER can be obtained  
819 from [https://www.temis.nl/surface/albedo/tropomi\\_ler.php](https://www.temis.nl/surface/albedo/tropomi_ler.php) (last access: 10 Nov 2024).

## 820 **Competing interests**

821 Bryan N. Duncan is a member of the editorial board of Atmospheric Chemistry and Physics

## 822 **Acknowledgements**

823 We thank all principal investigators, pilots, and managers who collected the aircraft data used in our  
824 research and made them publicly available. We thank the FTIR HCHO measurement team of Thomas  
825 Blumenstock, Martine De Mazière, Michel Grutter, James W. Hannigan, Nicholas Jones, Rigel Kivi, Erik  
826 Lutsch, Emmanuel Mahieu, Maria Makarova, Isamu Morino, Isao Murata, Tomoo Nagahama, Justus  
827 Notholt, Ivan Ortega, Mathias Palm, Amelie Röhlting, Matthias Schneider, Dan Smale, Wolfgang Stremme,  
828 Kim String, Youwen Sun, Ralf Sussmann, Yao Té, and Pucal Wang. We thank the Meteorological Service  
829 Suriname and Cornelis Becker for their support. The MAX-DOAS data used in this publication were  
830 obtained from Alkis Bais, John Burrows, Ka Lok Chan, Michel Grutter, Cheng Liu, Hitoshi Irie, Vinod  
831 Kumar, Yugo Kanaya, Ankie Pitters, Claudia Rivera-Cárdenas, Andreas Richter, Michel Van Roozendael,  
832 Robert Ryan, Vinayak Sinha, and Thomas Wagner. Fast delivery of MAX-DOAS data tailored to the S5P  
833 validation was organized through S5PVT AO project NID-FORVAL. We thank the IISER Mohali  
834 atmospheric chemistry facility for supporting the MAX-DOAS measurements at Mohali, India. We thank  
835 Julie M. Nicely for providing merged ATOMs observations.

## 836 **Authors' contributions**

837 AHS designed and implemented the research idea, analyzed the data, made all figures, and wrote the  
838 manuscript. TV, CV, GP, SC, and BL provided the paired TROPOMI and benchmark data. Other authors  
839 helped with the analysis, the model setup, and interpretation.

## 840 **References:**

- 841 Ahamad, F., Griffiths, P. T., Latif, M. T., Juneng, L., and Xiang, C. J.: Ozone Trends from Two Decades of  
842 Ground Level Observation in Malaysia, *Atmosphere*, 11, 755,  
843 <https://doi.org/10.3390/atmos11070755>, 2020.
- 844 Anderson, D. C., Follette-Cook, M. B., Strode, S. A., Nicely, J. M., Liu, J., Ivatt, P. D., and Duncan, B.  
845 N.: A machine learning methodology for the generation of a parameterization of the hydroxyl radical,  
846 *Geosci. Model Dev.*, 15, 6341–6358, <https://doi.org/10.5194/gmd-15-6341-2022>, 2022.
- 847 Archibald, A. T., Jenkin, M. E., and Shallcross, D. E.: An isoprene mechanism intercomparison, *Atmos.*  
848 *Environ.*, 44, 5356–5364, <https://doi.org/10.1016/j.atmosenv.2009.09.016>, 2010.
- 849 Baylon, P., Jaffe, D. A., Hall, S. R., Ullmann, K., Alvarado, M. J., and Lefer, B. L.: Impact of Biomass  
850 Burning Plumes on Photolysis Rates and Ozone Formation at the Mount Bachelor Observatory, *J.*  
851 *Geophys. Res. Atmos.*, 123, 2272–2284, <https://doi.org/10.1002/2017JD027341>, 2018.

- 852 Beddows, D. C. S., Dall'Osto, M., and Harrison, R. M.: Cluster Analysis of Rural, Urban, and Curbside  
853 Atmospheric Particle Size Data, *Environ. Sci. Technol.*, 43, 4694–4700,  
854 <https://doi.org/10.1021/es803121t>, 2009.
- 855 Belhout, D., Kerbachi, R., Relvas, H., and Miranda, A. I.: Air quality assessment in Algiers city, *Air*  
856 *Qual. Atmos. Health.*, 11, 897–906, <https://doi.org/10.1007/s11869-018-0589-x>, 2018.
- 857 Boraïy, M., El-Metwally, M., Wheida, A., El-Nazer, M., Hassan, S. K., El-Sanabary, F. F., Alfaro, S. C.,  
858 Abdelwahab, M., and Borbon, A.: Statistical analysis of the variability of reactive trace gases (SO<sub>2</sub>,  
859 NO<sub>2</sub> and ozone) in Greater Cairo during dust storm events, *J. Atmos. Chem.*, 80, 227–250,  
860 <https://doi.org/10.1007/s10874-023-09449-4>, 2023.
- 861 Bottorff, B., Lew, M. M., Woo, Y., Rickly, P., Rollings, M. D., Deming, B., Anderson, D. C., Wood, E.,  
862 Alwe, H. D., Millet, D. B., Weinheimer, A., Tyndall, G., Ortega, J., Dusanter, S., Leonardis, T., Flynn,  
863 J., Erickson, M., Alvarez, S., Rivera-Rios, J. C., Shutter, J. D., Keutsch, F., Helmig, D., Wang, W.,  
864 Allen, H. M., Slade, J. H., Shepson, P. B., Bertman, S., and Stevens, P. S.: OH, HO<sub>2</sub>, and RO<sub>2</sub> radical  
865 chemistry in a rural forest environment: measurements, model comparisons, and evidence of a  
866 missing radical sink, *Atmos. Chem. Phys.*, 23, 10287–10311, [https://doi.org/10.5194/acp-23-10287-](https://doi.org/10.5194/acp-23-10287-2023)  
867 [2023](https://doi.org/10.5194/acp-23-10287-2023), 2023.
- 868 Brune, W. H., Miller, D. O., Thames, A. B., Allen, H. M., Apel, E. C., Blake, D. R., Bui, T. P., Commane,  
869 R., Crounse, J. D., Daube, B. C., Diskin, G. S., DiGangi, J. P., Elkins, J. W., Hall, S. R., Hanisco, T.  
870 F., Hannun, R. A., Hintsä, E. J., Hornbrook, R. S., Kim, M. J., McKain, K., Moore, F. L., Neuman, J.  
871 A., Nicely, J. M., Peischl, J., Ryerson, T. B., St. Clair, J. M., Sweeney, C., Teng, A. P., Thompson, C.,  
872 Ullmann, K., Veres, P. R., Wennberg, P. O., and Wolfe, G. M.: Exploring Oxidation in the Remote  
873 Free Troposphere: Insights From Atmospheric Tomography (ATom), *J. Geophys. Res. Atmos.*, 125,  
874 [e2019JD031685](https://doi.org/10.1029/2019JD031685), <https://doi.org/10.1029/2019JD031685>, 2020.
- 875 Brune, W. H., Miller, D. O., Thames, A. B., Brosius, A. L., Barletta, B., Blake, D. R., Blake, N. J., Chen,  
876 G., Choi, Y., Crawford, J. H., Digangi, J. P., Diskin, G., Fried, A., Hall, S. R., Hanisco, T. F., Huey, G.  
877 L., Hughes, S. C., Kim, M., Meinardi, S., Montzka, D. D., Pusede, S. E., Schroeder, J. R., Teng, A.,  
878 Tanner, D. J., Ullmann, K., Walega, J., Weinheimer, A., Wisthaler, A., and Wennberg, P. O.:  
879 Observations of atmospheric oxidation and ozone production in South Korea, *Atmos. Environ.*, 269,  
880 [118854](https://doi.org/10.1016/j.atmosenv.2021.118854), <https://doi.org/10.1016/j.atmosenv.2021.118854>, 2022.
- 881 Cazorla, M. and Brune, W. H.: Measurement of Ozone Production Sensor, *Atmos. Meas. Tech.*, 3, 545–  
882 [555](https://doi.org/10.5194/amt-3-545-2010), <https://doi.org/10.5194/amt-3-545-2010>, 2010.
- 883 Cazorla, M., Brune, W. H., Ren, X., and Lefer, B.: Direct measurement of ozone production rates in  
884 Houston in 2009 and comparison with two estimation methods, *Atmos. Chem. Phys.*, 12, 1203–1212,  
885 <https://doi.org/10.5194/acp-12-1203-2012>, 2012.
- 886 Chaichan, M. T., Kazem, H. A., and Abed, T. A.: Traffic and outdoor air pollution levels near highways in  
887 Baghdad, Iraq, *Environ. Dev. Sustain.*, 20, 589–603, <https://doi.org/10.1007/s10668-016-9900-x>,  
888 2018.
- 889 Chatfield, R. B., Ren, X., Brune, W., and Schwab, J.: Controls on urban ozone production rate as  
890 indicated by formaldehyde oxidation rate and nitric oxide, *Atmos. Environ.*, 44, 5395–5406,  
891 <https://doi.org/10.1016/j.atmosenv.2010.08.056>, 2010.
- 892 Choi, J., Henze, D. K., Cao, H., Nowlan, C. R., González Abad, G., Kwon, H.-A., Lee, H.-M., Oak, Y. J.,  
893 Park, R. J., Bates, K. H., Maasackers, J. D., Wisthaler, A., and Weinheimer, A. J.: An Inversion  
894 Framework for Optimizing Non-Methane VOC Emissions Using Remote Sensing and Airborne

- 895 Observations in Northeast Asia During the KORUS-AQ Field Campaign, *J. Geophys. Res. Atmos.*,  
896 127, e2021JD035844, <https://doi.org/10.1029/2021JD035844>, 2022.
- 897 Choi, S., Lamsal, L. N., Follette-Cook, M., Joiner, J., Krotkov, N. A., Swartz, W. H., Pickering, K. E.,  
898 Loughner, C. P., Appel, W., Pfister, G., Saide, P. E., Cohen, R. C., Weinheimer, A. J., and Herman, J.  
899 R.: Assessment of NO<sub>2</sub> observations during DISCOVER-AQ and KORUS-AQ field campaigns,  
900 *Atmos. Meas. Tech.*, 13, 2523–2546, <https://doi.org/10.5194/amt-13-2523-2020>, 2020.
- 901 Choi, Y. and Souri, A. H.: Chemical condition and surface ozone in large cities of Texas during the last  
902 decade: Observational evidence from OMI, CAMS, and model analysis, *Remote Sens. Environ.*, 168,  
903 90–101, <https://doi.org/10.1016/j.rse.2015.06.026>, 2015a.
- 904 Choi, Y. and Souri, A. H.: Seasonal behavior and long-term trends of tropospheric ozone, its precursors  
905 and chemical conditions over Iran: A view from space, *Atmos. Environ.*, 106, 232–240,  
906 <https://doi.org/10.1016/j.atmosenv.2015.02.012>, 2015b.
- 907 Choi, Y., Kim, H., Tong, D., and Lee, P.: Summertime weekly cycles of observed and modeled NO<sub>x</sub> and  
908 O<sub>3</sub> concentrations as a function of satellite-derived ozone production sensitivity and land use types  
909 over the Continental United States, *Atmos. Chem. Phys.*, 12, 6291–6307, <https://doi.org/10.5194/acp-12-6291-2012>, 2012.
- 911 Colombi, N. K., Jacob, D. J., Yang, L. H., Zhai, S., Shah, V., Grange, S. K., Yantosca, R. M., Kim, S., and  
912 Liao, H.: Why is ozone in South Korea and the Seoul metropolitan area so high and increasing?,  
913 *Atmos. Chem. Phys.*, 23, 4031–4044, <https://doi.org/10.5194/acp-23-4031-2023>, 2023.
- 914 Crawford, J. H., Ahn, J.-Y., Al-Saadi, J., Chang, L., Emmons, L. K., Kim, J., Lee, G., Park, J.-H., Park, R.  
915 J., Woo, J. H., Song, C.-K., Hong, J.-H., Hong, Y.-D., Lefer, B. L., Lee, M., Lee, T., Kim, S., Min, K.-  
916 E., Yum, S. S., Shin, H. J., Kim, Y.-W., Choi, J.-S., Park, J.-S., Szykman, J. J., Long, R. W., Jordan, C.  
917 E., Simpson, I. J., Fried, A., Dibb, J. E., Cho, S., and Kim, Y. P.: The Korea–United States Air Quality  
918 (KORUS-AQ) field study, *Elem. Sci. Anth.*, 9, 00163, <https://doi.org/10.1525/elementa.2020.00163>,  
919 2021.
- 920 De Smedt, I., Pinardi, G., Vigouroux, C., Compernelle, S., Bais, A., Benavent, N., Boersma, F., Chan, K.-  
921 L., Donner, S., Eichmann, K.-U., Hedelt, P., Hendrick, F., Irie, H., Kumar, V., Lambert, J.-C.,  
922 Langerock, B., Lerot, C., Liu, C., Loyola, D., Piters, A., Richter, A., Rivera Cárdenas, C., Romahn, F.,  
923 Ryan, R. G., Sinha, V., Theys, N., Vlietinck, J., Wagner, T., Wang, T., Yu, H., and Van Roozendaal,  
924 M.: Comparative assessment of TROPOMI and OMI formaldehyde observations and validation  
925 against MAX-DOAS network column measurements, *Atmos. Chem. Phys.*, 21, 12561–12593,  
926 <https://doi.org/10.5194/acp-21-12561-2021>, 2021.
- 927 DiMaria, C. A., Jones, D. B. A., Worden, H., Bloom, A. A., Bowman, K., Stavrou, T., Miyazaki, K.,  
928 Worden, J., Guenther, A., Sarkar, C., Seco, R., Park, J.-H., Tota, J., Alves, E. G., and Ferracci, V.:  
929 Optimizing the Isoprene Emission Model MEGAN With Satellite and Ground-Based Observational  
930 Constraints, *J. Geophys. Res. Atmos.*, 128, e2022JD037822, <https://doi.org/10.1029/2022JD037822>,  
931 2023.
- 932 Duncan, B. N. and Chameides, W. L.: Effects of urban emission control strategies on the export of ozone  
933 and ozone precursors from the urban atmosphere to the troposphere, *J. Geophys. Res. Atmos.*, 103,  
934 28159–28179, <https://doi.org/10.1029/98JD02145>, 1998.
- 935 Duncan, B. N., Strahan, S. E., Yoshida, Y., Steenrod, S. D., and Livesey, N.: Model study of the cross-  
936 tropopause transport of biomass burning pollution, *Atmos. Chem. Phys.*, 7, 3713–3736,  
937 <https://doi.org/10.5194/acp-7-3713-2007>, 2007.



- 938 Duncan, B. N., Yoshida, Y., Olson, J. R., Sillman, S., Martin, R. V., Lamsal, L., Hu, Y., Pickering, K. E.,  
 939 Retscher, C., Allen, D. J., and Crawford, J. H.: Application of OMI observations to a space-based  
 940 indicator of NO<sub>x</sub> and VOC controls on surface ozone formation, *Atmos. Environ.*, 44, 2213–2223,  
 941 <https://doi.org/10.1016/j.atmosenv.2010.03.010>, 2010.
- 942 Fleming, Z. L., Doherty, R. M., von Schneidemesser, E., Malley, C. S., Cooper, O. R., Pinto, J. P., Colette,  
 943 A., Xu, X., Simpson, D., Schultz, M. G., Lefohn, A. S., Hamad, S., Moolla, R., Solberg, S., and Feng,  
 944 Z.: Tropospheric Ozone Assessment Report: Present-day ozone distribution and trends relevant to  
 945 human health, *Elem. Sci. Anth.*, 6, 12, <https://doi.org/10.1525/elementa.273>, 2018.
- 946 Gaudel, A., Cooper, O. R., Ancellet, G., Barret, B., Boynard, A., Burrows, J. P., Clerbaux, C., Coheur, P.-  
 947 F., Cuesta, J., Cuevas, E., Doniki, S., Dufour, G., Ebojje, F., Foret, G., Garcia, O., Granados-Muñoz,  
 948 M. J., Hannigan, J. W., Hase, F., Hassler, B., Huang, G., Hurtmans, D., Jaffe, D., Jones, N.,  
 949 Kalabokas, P., Kerridge, B., Kulawik, S., Latter, B., Leblanc, T., Le Flochmoën, E., Lin, W., Liu, J.,  
 950 Liu, X., Mahieu, E., McClure-Begley, A., Neu, J. L., Osman, M., Palm, M., Petetin, H.,  
 951 Petropavlovskikh, I., Querel, R., Rahpoe, N., Rozanov, A., Schultz, M. G., Schwab, J., Siddans, R.,  
 952 Smale, D., Steinbacher, M., Tanimoto, H., Tarasick, D. W., Thouret, V., Thompson, A. M., Trickl, T.,  
 953 Weatherhead, E., Wespes, C., Worden, H. M., Vigouroux, C., Xu, X., Zeng, G., and Ziemke, J.:  
 954 Tropospheric Ozone Assessment Report: Present-day distribution and trends of tropospheric ozone  
 955 relevant to climate and global atmospheric chemistry model evaluation, *Elem. Sci. Anth.*, 6, 39,  
 956 <https://doi.org/10.1525/elementa.291>, 2018.
- 957 Gerasopoulos, E., Kouvarakis, G., Vrekoussis, M., Donoussis, C., Mihalopoulos, N., and Kanakidou, M.:  
 958 Photochemical ozone production in the Eastern Mediterranean, *Atmos. Environ.*, 40, 3057–3069,  
 959 <https://doi.org/10.1016/j.atmosenv.2005.12.061>, 2006.
- 960 Govender, P. and Sivakumar, V.: Application of k-means and hierarchical clustering techniques for  
 961 analysis of air pollution: A review (1980–2019), *Atmos. Pollut. Res.*, 11, 40–56,  
 962 <https://doi.org/10.1016/j.apr.2019.09.009>, 2020.
- 963 Jeon, W., Choi, Y., Souri, A. H., Roy, A., Diao, L., Pan, S., Lee, H. W., and Lee, S.-H.: Identification of  
 964 chemical fingerprints in long-range transport of burning induced upper tropospheric ozone from  
 965 Colorado to the North Atlantic Ocean, *Sci. Total Environ.*, 613–614, 820–828,  
 966 <https://doi.org/10.1016/j.scitotenv.2017.09.177>, 2018.
- 967 Jin, X., Fiore, A. M., Murray, L. T., Valin, L. C., Lamsal, L. N., Duncan, B., Folkert Boersma, K., De  
 968 Smedt, I., Abad, G. G., Chance, K., and Tonnesen, G. S.: Evaluating a Space-Based Indicator of  
 969 Surface Ozone-NO<sub>x</sub>-VOC Sensitivity Over Midlatitude Source Regions and Application to Decadal  
 970 Trends, *J. Geophys. Res. Atmos.*, 122, 10,439-10,461, <https://doi.org/10.1002/2017JD026720>, 2017.
- 971 Johnson, M. S., Souri, A. H., Philip, S., Kumar, R., Naeger, A., Geddes, J., Judd, L., Janz, S., Chong, H.,  
 972 and Sullivan, J.: Satellite remote-sensing capability to assess tropospheric-column ratios of  
 973 formaldehyde and nitrogen dioxide: case study during the Long Island Sound Tropospheric Ozone  
 974 Study 2018 (LISTOS 2018) field campaign, *Atmos. Meas. Tech.*, 16, 2431–2454,  
 975 <https://doi.org/10.5194/amt-16-2431-2023>, 2023.
- 976 Kim, S.-W., McDonald, B. C., Seo, S., Kim, K.-M., and Trainer, M.: Understanding the Paths of Surface  
 977 Ozone Abatement in the Los Angeles Basin, *J. Geophys. Res. Atmos.*, 127, e2021JD035606,  
 978 <https://doi.org/10.1029/2021JD035606>, 2022.
- 979 Kleinman, L. I., Daum, P. H., Imre, D., Lee, Y.-N., Nunnermacker, L. J., Springston, S. R., Weinstein-  
 980 Lloyd, J., and Rudolph, J.: Ozone production rate and hydrocarbon reactivity in 5 urban areas: A  
 981 cause of high ozone concentration in Houston, *Geophys. Res. Lett.*, 29, 105-1-105-4,  
 982 <https://doi.org/10.1029/2001GL014569>, 2002.

- 983 Kusumaningtyas, S. D. A., Tonokura, K., Muharsyah, R., Gunawan, D., Sopaheluwakan, A., Iriana, W.,  
984 Lestari, P., Permadi, D. A., Rahmawati, R., and Samputra, N. A. R.: Comprehensive analysis of long-  
985 term trends, meteorological influences, and ozone formation sensitivity in the Jakarta Greater Area,  
986 *Sci. Rep.*, 14, 9605, <https://doi.org/10.1038/s41598-024-60374-2>, 2024.
- 987 Lelieveld, J., Hoor, P., Jöckel, P., Pozzer, A., Hadjinicolaou, P., Cammas, J.-P., and Beirle, S.: Severe  
988 ozone air pollution in the Persian Gulf region, *Atmos. Chem. Phys.*, 9, 1393–1406,  
989 <https://doi.org/10.5194/acp-9-1393-2009>, 2009.
- 990 Li, K., Jacob, D. J., Liao, H., Shen, L., Zhang, Q., and Bates, K. H.: Anthropogenic drivers of 2013–2017  
991 trends in summer surface ozone in China, *Proc. Natl. Acad. Sci.*, 116, 422–427,  
992 <https://doi.org/10.1073/pnas.1812168116>, 2019.
- 993 Marais, E. A., Jacob, D. J., Guenther, A., Chance, K., Kurosu, T. P., Murphy, J. G., Reeves, C. E., and  
994 Pye, H. O. T.: Improved model of isoprene emissions in Africa using Ozone Monitoring Instrument  
995 (OMI) satellite observations of formaldehyde: implications for oxidants and particulate matter,  
996 *Atmos. Chem. Phys.*, 14, 7693–7703, <https://doi.org/10.5194/acp-14-7693-2014>, 2014.
- 997 Martin, R. V., Fiore, A. M., and Van Donkelaar, A.: Space-based diagnosis of surface ozone sensitivity to  
998 anthropogenic emissions, *Geophys. Res. Lett.*, 31, <https://doi.org/10.1029/2004GL019416>, 2004.
- 999 Marvin, M. R., Wolfe, G. M., Salawitch, R. J., Canty, T. P., Roberts, S. J., Travis, K. R., Aikin, K. C., de  
1000 Gouw, J. A., Graus, M., Hanisco, T. F., Holloway, J. S., Hübler, G., Kaiser, J., Keutsch, F. N., Peischl,  
1001 J., Pollack, I. B., Roberts, J. M., Ryerson, T. B., Veres, P. R., and Warneke, C.: Impact of evolving  
1002 isoprene mechanisms on simulated formaldehyde: An inter-comparison supported by in situ  
1003 observations from SENEX, *Atmos. Environ.*, 164, 325–336,  
1004 <https://doi.org/10.1016/j.atmosenv.2017.05.049>, 2017.
- 1005 Mazzuca, G. M., Ren, X., Loughner, C. P., Estes, M., Crawford, J. H., Pickering, K. E., Weinheimer, A. J.,  
1006 and Dickerson, R. R.: Ozone production and its sensitivity to NO<sub>x</sub> and VOCs: results from the  
1007 DISCOVER-AQ field experiment, Houston 2013, *Atmos. Chem. Phys.*, 16, 14463–14474,  
1008 <https://doi.org/10.5194/acp-16-14463-2016>, 2016.
- 1009 Miller, D. O. and Brune, W. H.: Investigating the Understanding of Oxidation Chemistry Using 20 Years  
1010 of Airborne OH and HO<sub>2</sub> Observations, *J. Geophys. Res. Atmos.*, 127, e2021JD035368,  
1011 <https://doi.org/10.1029/2021JD035368>, 2022.
- 1012 Mills, G., Pleijel, H., Malley, C. S., Sinha, B., Cooper, O. R., Schultz, M. G., Neufeld, H. S., Simpson, D.,  
1013 Sharps, K., Feng, Z., Gerosa, G., Harmens, H., Kobayashi, K., Saxena, P., Paoletti, E., Sinha, V., and  
1014 Xu, X.: Tropospheric Ozone Assessment Report: Present-day tropospheric ozone distribution and  
1015 trends relevant to vegetation, *Elem. Sci. Anth.*, 6, 47, <https://doi.org/10.1525/elementa.302>, 2018.
- 1016 Miyazaki, K., Eskes, H., Sudo, K., Boersma, K. F., Bowman, K., and Kanaya, Y.: Decadal changes in  
1017 global surface NO<sub>x</sub> emissions from multi-constituent satellite data assimilation, *Atmos. Chem. Phys.*,  
1018 17, 807–837, <https://doi.org/10.5194/acp-17-807-2017>, 2017.
- 1019 Orbe, C., Oman, L. D., Strahan, S. E., Waugh, D. W., Pawson, S., Takacs, L. L., and Molod, A. M.: Large-  
1020 Scale Atmospheric Transport in GEOS Replay Simulations, *J. Adv. Model. Earth Syst.*, 9, 2545–2560,  
1021 <https://doi.org/10.1002/2017MS001053>, 2017.
- 1022 Pan, S., Roy, A., Choi, Y., Eslami, E., Thomas, S., Jiang, X., and Gao, H. O.: Potential impacts of electric  
1023 vehicles on air quality and health endpoints in the Greater Houston Area in 2040, *Atmos. Environ.*,  
1024 207, 38–51, <https://doi.org/10.1016/j.atmosenv.2019.03.022>, 2019.

- 1025 Ren, X., van Duin, D., Cazorla, M., Chen, S., Mao, J., Zhang, L., Brune, W. H., Flynn, J. H., Grossberg,  
1026 N., Lefer, B. L., Rappenglück, B., Wong, K. W., Tsai, C., Stutz, J., Dibb, J. E., Thomas Jobson, B.,  
1027 Luke, W. T., and Kelley, P.: Atmospheric oxidation chemistry and ozone production: Results from  
1028 SHARP 2009 in Houston, Texas, *J. Geophys. Res. Atmos.*, 118, 5770–5780,  
1029 <https://doi.org/10.1002/jgrd.50342>, 2013.
- 1030 Roberts, G., Wooster, M. J., and Lagoudakis, E.: Annual and diurnal african biomass burning temporal  
1031 dynamics, *Biogeosciences*, 6, 849–866, <https://doi.org/10.5194/bg-6-849-2009>, 2009.
- 1032 Sadanaga, Y., Kawasaki, S., Tanaka, Y., Kajii, Y., and Bandow, H.: New System for Measuring the  
1033 Photochemical Ozone Production Rate in the Atmosphere, *Environ. Sci. Technol.*, 51, 2871–2878,  
1034 <https://doi.org/10.1021/acs.est.6b04639>, 2017.
- 1035 Sakamoto, Y., Shoji, K., Bui, M. T., Phạm, T. H., Vu, T. A., Ly, B. T., and Kajii, Y.: Air quality study in  
1036 Hanoi, Vietnam in 2015–2016 based on a one-year observation of NO<sub>x</sub>, O<sub>3</sub>, CO and a one-week  
1037 observation of VOCs, *Atmos. Pollut. Res.*, 9, 544–551, <https://doi.org/10.1016/j.apr.2017.12.001>,  
1038 2018.
- 1039 Schroeder, J. R., Crawford, J. H., Ahn, J.-Y., Chang, L., Fried, A., Walega, J., Weinheimer, A., Montzka,  
1040 D. D., Hall, S. R., Ullmann, K., Wisthaler, A., Mikoviny, T., Chen, G., Blake, D. R., Blake, N. J.,  
1041 Hughes, S. C., Meinardi, S., Diskin, G., Digangi, J. P., Choi, Y., Pusede, S. E., Huey, G. L., Tanner, D.  
1042 J., Kim, M., and Wennberg, P.: Observation-based modeling of ozone chemistry in the Seoul  
1043 metropolitan area during the Korea-United States Air Quality Study (KORUS-AQ), *Elem. Sci. Anth.*,  
1044 8, 3, <https://doi.org/10.1525/elementa.400>, 2020.
- 1045 Schroeder, J. R., Crawford, J. H., Fried, A., Walega, J., Weinheimer, A., Wisthaler, A., Müller, M.,  
1046 Mikoviny, T., Chen, G., Shook, M., Blake, D. R., and Tonnesen, G. S.: New insights into the column  
1047 CH<sub>2</sub>O/NO<sub>2</sub> ratio as an indicator of near-surface ozone sensitivity, *J. Geophys. Res. Atmos.*, 122,  
1048 8885–8907, <https://doi.org/10.1002/2017JD026781>, 2017.
- 1049 Sillman, S. and He, D.: Some theoretical results concerning O<sub>3</sub>-NO<sub>x</sub>-VOC chemistry and NO<sub>x</sub>-VOC  
1050 indicators, *J. Geophys. Res. Atmos.*, 107, ACH 26-1-ACH 26-15,  
1051 <https://doi.org/10.1029/2001JD001123>, 2002.
- 1052 Silva, S. J., Heald, C. L., Ravela, S., Mammarella, I., and Munger, J. W.: A Deep Learning  
1053 Parameterization for Ozone Dry Deposition Velocities, *Geophys. Res. Lett.*, 46, 983–989,  
1054 <https://doi.org/10.1029/2018GL081049>, 2019.
- 1055 Simpson, W. R., Brown, S. S., Saiz-Lopez, A., Thornton, J. A., and von Glasow, R.: Tropospheric  
1056 Halogen Chemistry: Sources, Cycling, and Impacts, *Chem. Rev.*, 115, 4035–4062,  
1057 <https://doi.org/10.1021/cr5006638>, 2015.
- 1058 Singh, H. B., Brune, W. H., Crawford, J. H., Flocke, F., and Jacob, D. J.: Chemistry and transport of  
1059 pollution over the Gulf of Mexico and the Pacific: spring 2006 INTEX-B campaign overview and  
1060 first results, *Atmos. Chem. Phys.*, 9, 2301–2318, <https://doi.org/10.5194/acp-9-2301-2009>, 2009.
- 1061 Sklaveniti, S., Locoge, N., Stevens, P. S., Wood, E., Kundu, S., and Dusanter, S.: Development of an  
1062 instrument for direct ozone production rate measurements: measurement reliability and current  
1063 limitations, *Atmos. Meas. Tech.*, 11, 741–761, <https://doi.org/10.5194/amt-11-741-2018>, 2018.
- 1064 Souri, A. H., Chance, K., Bak, J., Nowlan, C. R., González Abad, G., Jung, Y., Wong, D. C., Mao, J., and  
1065 Liu, X.: Unraveling pathways of elevated ozone induced by the 2020 lockdown in Europe by an  
1066 observationally constrained regional model using TROPOMI, *Atmos. Chem. Phys.*, 21, 18227–18245,  
1067 <https://doi.org/10.5194/acp-21-18227-2021>, 2021.

- 1068 Souri, A. H., Choi, Y., Jeon, W., Li, X., Pan, S., Diao, L., and Westenbarger, D. A.: Constraining NO<sub>x</sub>  
 1069 emissions using satellite NO<sub>2</sub> measurements during 2013 DISCOVER-AQ Texas campaign, *Atmos.*  
 1070 *Environ.*, 131, 371–381, <https://doi.org/10.1016/j.atmosenv.2016.02.020>, 2016a.
- 1071 Souri, A. H., Choi, Y., Li, X., Kotsakis, A., and Jiang, X.: A 15-year climatology of wind pattern impacts  
 1072 on surface ozone in Houston, Texas, *Atmos. Res.*, 174–175, 124–134,  
 1073 <https://doi.org/10.1016/j.atmosres.2016.02.007>, 2016b.
- 1074 Souri, A. H., Duncan, B. N., Strode, S. A., Anderson, D. C., Manyin, M. E., Liu, J., Oman, L. D., Zhang,  
 1075 Z., and Weir, B.: Enhancing Long-Term Trend Simulation of Global Tropospheric OH and Its Drivers  
 1076 from 2005-2019: A Synergistic Integration of Model Simulations and Satellite Observations,  
 1077 *EGU*sphere, 1–37, <https://doi.org/10.5194/egusphere-2024-410>, 2024.
- 1078 Souri, A. H., Johnson, M. S., Wolfe, G. M., Crawford, J. H., Fried, A., Wisthaler, A., Brune, W. H., Blake,  
 1079 D. R., Weinheimer, A. J., Verhoelst, T., Compernelle, S., Pinardi, G., Vigouroux, C., Langerock, B.,  
 1080 Choi, S., Lamsal, L., Zhu, L., Sun, S., Cohen, R. C., Min, K.-E., Cho, C., Philip, S., Liu, X., and  
 1081 Chance, K.: Characterization of errors in satellite-based HCHO/NO<sub>2</sub> tropospheric column ratios with  
 1082 respect to chemistry, column-to-PBL translation, spatial representation, and retrieval uncertainties,  
 1083 *Atmos. Chem. Phys.*, 23, 1963–1986, <https://doi.org/10.5194/acp-23-1963-2023>, 2023.
- 1084 Souri, A. H., Nowlan, C. R., González Abad, G., Zhu, L., Blake, D. R., Fried, A., Weinheimer, A. J.,  
 1085 Wisthaler, A., Woo, J.-H., Zhang, Q., Chan Miller, C. E., Liu, X., and Chance, K.: An inversion of  
 1086 NO<sub>x</sub> and non-methane volatile organic compound (NMVOC) emissions using satellite observations  
 1087 during the KORUS-AQ campaign and implications for surface ozone over East Asia, *Atmos. Chem.*  
 1088 *Phys.*, 20, 9837–9854, <https://doi.org/10.5194/acp-20-9837-2020>, 2020b.
- 1089 Souri, A. H., Nowlan, C. R., Wolfe, G. M., Lamsal, L. N., Chan Miller, C. E., Abad, G. G., Janz, S. J.,  
 1090 Fried, A., Blake, D. R., Weinheimer, A. J., Diskin, G. S., Liu, X., and Chance, K.: Revisiting the  
 1091 effectiveness of HCHO/NO<sub>2</sub> ratios for inferring ozone sensitivity to its precursors using high  
 1092 resolution airborne remote sensing observations in a high ozone episode during the KORUS-AQ  
 1093 campaign, *Atmos. Environ.*, 224, 117341, <https://doi.org/10.1016/j.atmosenv.2020.117341>, 2020a.
- 1094 Stanier, C. O., Pierce, R. B., Abdi-Oskouei, M., Adelman, Z. E., Al-Saadi, J., Alwe, H. D., Bertram, T. H.,  
 1095 Carmichael, G. R., Christiansen, M. B., Cleary, P. A., Czarnetzki, A. C., Dickens, A. F., Fuoco, M. A.,  
 1096 Hughes, D. D., Hupy, J. P., Janz, S. J., Judd, L. M., Kenski, D., Kowalewski, M. G., Long, R. W.,  
 1097 Millet, D. B., Novak, G., Roozitalab, B., Shaw, S. L., Stone, E. A., Szykman, J., Valin, L., Vermeuel,  
 1098 M., Wagner, T. J., Whitehill, A. R., and Williams, D. J.: Overview of the Lake Michigan Ozone Study  
 1099 2017, *Bull. Am. Meteorol. Soc.*, 102, E2207–E2225, <https://doi.org/10.1175/BAMS-D-20-0061.1>,  
 1100 2021.
- 1101 Stavrakou, T., Müller, J.-F., Bauwens, M., De Smedt, I., Lerot, C., Van Roozendaal, M., Coheur, P.-F.,  
 1102 Clerbaux, C., Boersma, K. F., van der A, R., and Song, Y.: Substantial Underestimation of Post-  
 1103 Harvest Burning Emissions in the North China Plain Revealed by Multi-Species Space Observations,  
 1104 *Sci. Rep.*, 6, 32307, <https://doi.org/10.1038/srep32307>, 2016.
- 1105 Strode, S. A., Ziemke, J. R., Oman, L. D., Lamsal, L. N., Olsen, M. A., and Liu, J.: Global changes in the  
 1106 diurnal cycle of surface ozone, *Atmos. Environ.*, 199, 323–333,  
 1107 <https://doi.org/10.1016/j.atmosenv.2018.11.028>, 2019.
- 1108 Tao, M., Fiore, A. M., Jin, X., Schiferl, L. D., Commane, R., Judd, L. M., Janz, S., Sullivan, J. T., Miller,  
 1109 P. J., Karambelas, A., Davis, S., Tzortziou, M., Valin, L., Whitehill, A., Civerolo, K., and Tian, Y.:  
 1110 Investigating Changes in Ozone Formation Chemistry during Summertime Pollution Events over the  
 1111 Northeastern United States, *Environ. Sci. Technol.*, 56, 15312–15327,  
 1112 <https://doi.org/10.1021/acs.est.2c02972>, 2022.



- 1113 Thompson, A. M., Balashov, N. V., Witte, J. C., Coetzee, J. G. R., Thouret, V., and Posny, F.:  
 1114 Tropospheric ozone increases over the southern Africa region: bellwether for rapid growth in  
 1115 Southern Hemisphere pollution?, *Atmos. Chem. Phys.*, 14, 9855–9869, [https://doi.org/10.5194/acp-](https://doi.org/10.5194/acp-14-9855-2014)  
 1116 14-9855-2014, 2014.
- 1117 Thompson, C. R., Wofsy, S. C., Prather, M. J., Newman, P. A., Hanisco, T. F., Ryerson, T. B., Fahey, D.  
 1118 W., Apel, E. C., Brock, C. A., Brune, W. H., Froyd, K., Katich, J. M., Nicely, J. M., Peischl, J., Ray,  
 1119 E., Veres, P. R., Wang, S., Allen, H. M., Asher, E., Bian, H., Blake, D., Bourgeois, I., Budney, J., Bui,  
 1120 T. P., Butler, A., Campuzano-Jost, P., Chang, C., Chin, M., Commane, R., Correa, G., Crouse, J. D.,  
 1121 Daube, B., Dibb, J. E., DiGangi, J. P., Diskin, G. S., Dollner, M., Elkins, J. W., Fiore, A. M., Flynn, C.  
 1122 M., Guo, H., Hall, S. R., Hannun, R. A., Hills, A., Hintsa, E. J., Hodzic, A., Hornbrook, R. S., Huey,  
 1123 L. G., Jimenez, J. L., Keeling, R. F., Kim, M. J., Kupc, A., Lacey, F., Lait, L. R., Lamarque, J.-F., Liu,  
 1124 J., McKain, K., Meinardi, S., Miller, D. O., Montzka, S. A., Moore, F. L., Morgan, E. J., Murphy, D.  
 1125 M., Murray, L. T., Nault, B. A., Neuman, J. A., Nguyen, L., González, Y., Rollins, A., Rosenlof, K.,  
 1126 Sargent, M., Schill, G., Schwarz, J. P., Clair, J. M. S., Steenrod, S. D., Stephens, B. B., Strahan, S. E.,  
 1127 Strode, S. A., Sweeney, C., Thames, A. B., Ullmann, K., Wagner, N., Weber, R., Weinzierl, B.,  
 1128 Wennberg, P. O., Williamson, C. J., Wolfe, G. M., and Zeng, L.: The NASA Atmospheric  
 1129 Tomography (ATom) Mission: Imaging the Chemistry of the Global Atmosphere, *Bull. Am. Meteorol.*  
 1130 *Soc.*, 103, E761–E790, <https://doi.org/10.1175/BAMS-D-20-0315.1>, 2022.
- 1131 Thornton, J. A., Wooldridge, P. J., Cohen, R. C., Martinez, M., Harder, H., Brune, W. H., Williams, E. J.,  
 1132 Roberts, J. M., Fehsenfeld, F. C., Hall, S. R., Shetter, R. E., Wert, B. P., and Fried, A.: Ozone  
 1133 production rates as a function of NO<sub>x</sub> abundances and HO<sub>x</sub> production rates in the Nashville urban  
 1134 plume, *J. Geophys. Res. Atmos.*, 107, ACH 7-1-ACH 7-17, <https://doi.org/10.1029/2001JD000932>,  
 1135 2002.
- 1136 Tibshirani, R.: Regression Shrinkage and Selection via the Lasso, *J. R. Stat. B (Methodological)*, 58, 267–  
 1137 288, 1996.
- 1138 Tilstra, L. G., de Graaf, M., Trees, V., Litvinov, P., Dubovik, O., and Stammes, P.: A directional surface  
 1139 reflectance climatology determined from TROPOMI observations, *Atmos. Meas. Tech. Discussions*,  
 1140 1–29, <https://doi.org/10.5194/amt-2023-222>, 2023.
- 1141 Tonnesen, G. S. and Dennis, R. L.: Analysis of radical propagation efficiency to assess ozone sensitivity  
 1142 to hydrocarbons and NO<sub>x</sub> : 1. Local indicators of instantaneous odd oxygen production sensitivity, *J.*  
 1143 *Geophys. Res.*, 105, 9213–9225, <https://doi.org/10.1029/1999JD900371>, 2000a.
- 1144 Tonnesen, G. S. and Dennis, R. L.: Analysis of radical propagation efficiency to assess ozone sensitivity  
 1145 to hydrocarbons and NO<sub>x</sub> : 2. Long-lived species as indicators of ozone concentration sensitivity, *J.*  
 1146 *Geophys. Res.*, 105, 9227–9241, <https://doi.org/10.1029/1999JD900372>, 2000b.
- 1147 van der Velde, I. R., van der Werf, G. R., Houweling, S., Eskes, H. J., Veefkind, J. P., Borsdorff, T., and  
 1148 Aben, I.: Biomass burning combustion efficiency observed from space using measurements of CO  
 1149 and NO<sub>2</sub> by the TROPospheric Monitoring Instrument (TROPOMI), *Atmos. Chem. Phys.*, 21, 597–  
 1150 616, <https://doi.org/10.5194/acp-21-597-2021>, 2021.
- 1151 van Geffen, J., Eskes, H., Compernelle, S., Pinardi, G., Verhoelst, T., Lambert, J.-C., Sneep, M., ter  
 1152 Linden, M., Ludewig, A., Boersma, K. F., and Veefkind, J. P.: Sentinel-5P TROPOMI NO<sub>2</sub> retrieval:  
 1153 impact of version v2.2 improvements and comparisons with OMI and ground-based data, *Atmos.*  
 1154 *Meas. Tech.*, 15, 2037–2060, <https://doi.org/10.5194/amt-15-2037-2022>, 2022.
- 1155 Veefkind, J. P., Aben, I., McMullan, K., Förster, H., de Vries, J., Otter, G., Claas, J., Eskes, H. J., de Haan,  
 1156 J. F., Kleipool, Q., van Weele, M., Hasekamp, O., Hoogeveen, R., Landgraf, J., Snel, R., Tol, P.,  
 1157 Ingmann, P., Voors, R., Kruizinga, B., Vink, R., Visser, H., and Levelt, P. F.: TROPOMI on the ESA

- 1158 Sentinel-5 Precursor: A GMES mission for global observations of the atmospheric composition for  
1159 climate, air quality and ozone layer applications, *Remote Sens. Environ.*, 120, 70–83,  
1160 <https://doi.org/10.1016/j.rse.2011.09.027>, 2012.
- 1161 Verhoelst, T., Compernelle, S., Pinardi, G., Lambert, J.-C., Eskes, H. J., Eichmann, K.-U., Fjæraa, A. M.,  
1162 Granville, J., Niemeijer, S., Cede, A., Tiefengraber, M., Hendrick, F., Pazmiño, A., Bais, A.,  
1163 Bazureau, A., Boersma, K. F., Bogner, K., Dehn, A., Donner, S., Elokhov, A., Gebetsberger, M.,  
1164 Goutail, F., Grutter de la Mora, M., Gruzdev, A., Gratsea, M., Hansen, G. H., Irie, H., Jepsen, N.,  
1165 Kanaya, Y., Karagkiozidis, D., Kivi, R., Kreher, K., Levelt, P. F., Liu, C., Müller, M., Navarro Comas,  
1166 M., PETERS, A. J. M., Pommereau, J.-P., Portafaix, T., Prados-Roman, C., Puentedura, O., Querel, R.,  
1167 Remmers, J., Richter, A., Rimmer, J., Rivera Cárdenas, C., Saavedra de Miguel, L., Sinyakov, V. P.,  
1168 Stremme, W., Strong, K., Van Roozendaal, M., Veeffkind, J. P., Wagner, T., Wittrock, F., Yela  
1169 González, M., and Zehner, C.: Ground-based validation of the Copernicus Sentinel-5P TROPOMI  
1170 NO<sub>2</sub> measurements with the NDACC ZSL-DOAS, MAX-DOAS and Pandora global networks,  
1171 *Atmos. Meas. Tech.*, 14, 481–510, <https://doi.org/10.5194/amt-14-481-2021>, 2021.
- 1172 Vigouroux, C., Langerock, B., Bauer Aquino, C. A., Blumenstock, T., Cheng, Z., De Mazière, M., De  
1173 Smedt, I., Grutter, M., Hannigan, J. W., Jones, N., Kivi, R., Loyola, D., Lutsch, E., Mahieu, E.,  
1174 Makarova, M., Metzger, J.-M., Morino, I., Murata, I., Nagahama, T., Notholt, J., Ortega, I., Palm, M.,  
1175 Pinardi, G., Röhlings, A., Smale, D., Stremme, W., Strong, K., Sussmann, R., Tè, Y., van Roozendaal,  
1176 M., Wang, P., and Winkler, H.: TROPOMI–Sentinel-5 Precursor formaldehyde validation using an  
1177 extensive network of ground-based Fourier-transform infrared stations, *Atmos. Meas. Tech.*, 13,  
1178 3751–3767, <https://doi.org/10.5194/amt-13-3751-2020>, 2020.
- 1179 Wang, T., Xue, L., Brimblecombe, P., Lam, Y. F., Li, L., and Zhang, L.: Ozone pollution in China: A  
1180 review of concentrations, meteorological influences, chemical precursors, and effects, *Sci. Total*  
1181 *Environ.*, 575, 1582–1596, <https://doi.org/10.1016/j.scitotenv.2016.10.081>, 2017.
- 1182 Wang, W., Parrish, D. D., Li, X., Shao, M., Liu, Y., Mo, Z., Lu, S., Hu, M., Fang, X., Wu, Y., Zeng, L.,  
1183 and Zhang, Y.: Exploring the drivers of the increased ozone production in Beijing in summertime  
1184 during 2005–2016, *Atmos. Chem. Phys.*, 20, 15617–15633, [https://doi.org/10.5194/acp-20-15617-](https://doi.org/10.5194/acp-20-15617-2020)  
1185 2020, 2020.
- 1186 Warneke, C., Trainer, M., de Gouw, J. A., Parrish, D. D., Fahey, D. W., Ravishankara, A. R., Middlebrook,  
1187 A. M., Brock, C. A., Roberts, J. M., Brown, S. S., Neuman, J. A., Lerner, B. M., Lack, D., Law, D.,  
1188 Hübler, G., Pollack, I., Sjostedt, S., Ryerson, T. B., Gilman, J. B., Liao, J., Holloway, J., Peischl, J.,  
1189 Nowak, J. B., Aikin, K. C., Min, K.-E., Washenfelder, R. A., Graus, M. G., Richardson, M.,  
1190 Markovic, M. Z., Wagner, N. L., Welti, A., Veres, P. R., Edwards, P., Schwarz, J. P., Gordon, T., Dube,  
1191 W. P., McKeen, S. A., Brioude, J., Ahmadov, R., Bougiatioti, A., Lin, J. J., Nenes, A., Wolfe, G. M.,  
1192 Hanisco, T. F., Lee, B. H., Lopez-Hilfiker, F. D., Thornton, J. A., Keutsch, F. N., Kaiser, J., Mao, J.,  
1193 and Hatch, C. D.: Instrumentation and measurement strategy for the NOAA SENEX aircraft  
1194 campaign as part of the Southeast Atmosphere Study 2013, *Atmos. Meas. Tech.*, 9, 3063–3093,  
1195 <https://doi.org/10.5194/amt-9-3063-2016>, 2016.
- 1196 Wolfe, G. M., Hanisco, T. F., Arkinson, H. L., Blake, D. R., Wisthaler, A., Mikoviny, T., Ryerson, T. B.,  
1197 Pollack, I., Peischl, J., Wennberg, P. O., Crouse, J. D., St. Clair, J. M., Teng, A., Huey, L. G., Liu, X.,  
1198 Fried, A., Weibring, P., Richter, D., Walega, J., Hall, S. R., Ullmann, K., Jimenez, J. L., Campuzano-  
1199 Jost, P., Bui, T. P., Diskin, G., Podolske, J. R., Sachse, G., and Cohen, R. C.: Photochemical evolution  
1200 of the 2013 California Rim Fire: synergistic impacts of reactive hydrocarbons and enhanced oxidants,  
1201 *Atmos. Chem. Phys.*, 22, 4253–4275, <https://doi.org/10.5194/acp-22-4253-2022>, 2022.

- 1202 Wolfe, G. M., Marvin, M. R., Roberts, S. J., Travis, K. R., and Liao, J.: The Framework for 0-D  
1203 Atmospheric Modeling (F0AM) v3.1, *Geosci. Model Dev.*, 9, 3309–3319,  
1204 <https://doi.org/10.5194/gmd-9-3309-2016>, 2016.
- 1205 Wu, Y., Zhao, K., Ren, X., Dickerson, R. R., Huang, J., Schwab, M. J., Stratton, P. R., Daley, H., Li, D.,  
1206 and Moshary, F.: Ozone pollution episodes and PBL height variation in the NYC urban and coastal  
1207 areas during LISTOS 2019, *Atmos. Environ.*, 320, 120317,  
1208 <https://doi.org/10.1016/j.atmosenv.2023.120317>, 2024.
- 1209 Xu, W., Zhang, G., Wang, Y., Tong, S., Zhang, W., Ma, Z., Lin, W., Kuang, Y., Yin, L., and Xu, X.:  
1210 Aerosol Promotes Peroxyacetyl Nitrate Formation During Winter in the North China Plain, *Environ.*  
1211 *Sci. Technol.*, 55, 3568–3581, <https://doi.org/10.1021/acs.est.0c08157>, 2021.
- 1212 Yousefian, F., Faridi, S., Azimi, F., Aghaei, M., Shamsipour, M., Yaghmaeian, K., and Hassanvand, M. S.:  
1213 Temporal variations of ambient air pollutants and meteorological influences on their concentrations in  
1214 Tehran during 2012–2017, *Sci. Rep.*, 10, 292, <https://doi.org/10.1038/s41598-019-56578-6>, 2020.
- 1215 Zara, M., Boersma, K. F., Eskes, H., Denier van der Gon, H., Vilà-Guerau de Arellano, J., Krol, M., van  
1216 der Swaluw, E., Schuch, W., and Velders, G. J. M.: Reductions in nitrogen oxides over the  
1217 Netherlands between 2005 and 2018 observed from space and on the ground: Decreasing emissions  
1218 and increasing O<sub>3</sub> indicate changing NO<sub>x</sub> chemistry, *Atmos. Environ.: X*, 9, 100104,  
1219 <https://doi.org/10.1016/j.aeaoa.2021.100104>, 2021.
- 1220 Zhang, J., Wang, T., Chameides, W. L., Cardelino, C., Kwok, J., Blake, D. R., Ding, A., and So, K. L.:  
1221 Ozone production and hydrocarbon reactivity in Hong Kong, Southern China, *Atmos. Chem. Phys.*, 7,  
1222 557–573, <https://doi.org/10.5194/acp-7-557-2007>, 2007.